Tonotopy is not preserved in a descending stage of auditory cortex

Miaoqing Gu[1,2,10], Shanshan Liang[3,10], Jiahui Zhu[2,3], Ruijie Li[3], Ke Liu[3], Xuanyue Wang[4], Frank Ohl[5,6,7], Yun Zhang[4], Xiang Liao[3,4], Chunqing Zhang[3], Hongbo Jia[1,5,9], Yi Zhou[2,8,*], Jianxiong Zhang[3,*], Xiaowei Chen[3,4,*]

[1]School of Physical Science and Technology, Guangxi University, Nanning 530004, China.

[2]Guangxi Key Laboratory of Special Biomedicine and Advanced Institute for Brain and Intelligence, School of Medicine, Guangxi University, Nanning, 530004, China

[3]Brain Research Center and State Key Laboratory of Trauma and Chemical Poisoning, Third Military Medical University, Chongqing 400038, China.

[4]Chongqing Institute for Brain and Intelligence, Guangyang Bay Laboratory, Chongqing 400064, China.

[5]Leibniz Institute for Neurobiology (LIN), Magdeburg, Germany.

[6]Insitute of Biology (IBIO), Otto-von-Guericke University, Magdeburg, Germany.

[7]Center for Behavioral Brain Sciences (CBBS), Magdeburg, Germany.

[8]Department of Neurobiology, Chongqing Key Laboratory of Neurobiology, School of Basic Medicine, Third Military Medical University, Chongqing 400038, China.

[9]Brain Research Instrument Innovation Center, Suzhou Institute of Biomedical Engineering and Technology, Chinese Academy of Sciences, Suzhou 215163, China

[10]These authors contributed equally to this work.

*Correspondence: yzhou@tmmu.edu.cn (Y.Z.), jianxiong_zhang1988@tmmu.edu.cn (J.Z.), xiaowei_chen@tmmu.edu.cn (X.C.)

Abstract

Previous studies based on layer specificity suggest that ascending signals from the thalamus to the sensory neocortex preserve spatially organized information, but it remains unknown whether sensory information descending from sensory neocortex to the thalamus also maintains such spatial organization pattern. By focusing on projection specificity, we mapped the tone response properties of two groups of cortical neurons in the primary auditory cortex (A1), based on the relationship between their specific connections to other regions and their function in ascending (thalamocortical recipient, TR neurons) or descending (corticothalamic, CT neurons) auditory information. A clear tonotopic gradient was observed among TR neurons, but not CT neurons. Additionally, CT neurons exhibited markedly higher heterogeneity in their frequency tuning and had broader bandwidth than TR neurons. These results reveal that the information flow descending from A1 to the thalamus via CT neurons is not arrange tonotopically, suggesting that the descending information flow possibly contributes to higher-order feedback processing of diverse auditory inputs.

Introduction

In the mammalian auditory system, one of the most prominent features is the tonotopic organization — a spatially ordered gradient of neuronal frequency preference (Bizley et al., 2005; Kajikawa et al., 2005; Merzenich et al., 1976; Morel et al., 1993; Nelken et al., 2004; Reale and Imig, 1980; Stiebler et al., 1997; Tani et al., 2018). Clear tonotopic maps have been found in the auditory cortex (AuC) of many mammalian species including humans (Clopton et al., 1974; Humphries et al., 2010), macaque monkeys (Hackett et al., 1998), cats (Lee et al., 2004), ferrets (Bizley et al., 2005), Mongolian gerbils (Budinger et al., 2000; Ohl et al., 2000; Thomas et al., 1993), rats (Polley et al., 2007), and mice (Guo et al., 2012; King et al., 2018). Tonotopy originates in the cochlea and is relayed and preserved throughout all the ascending stages, including the medial geniculate body (MGB) and the AuC (Jasmin et al., 2019; Simon et al., 2009; Smith and Wever, 1949). As one of the most explored pathways in

the auditory system, the connections between MGB and AuC play an essential role in the perception of auditory information (Lee, 2013; Ohga et al., 2017; Pardi et al., 2020).

Core fields of the AuC receive their predominant thalamic input from the ventral division of the MGB (MGBv), which confers well-defined frequency tuning arranged into smoothly varying tonotopic gradients (Andersen et al., 1980; Merzenich and Brugge, 1973; Winer et al., 2005). Non-core AuC fields are innervated by non-primary divisions of the MGB and from intracortical inputs originating outside of the AuC (Jones, 2001; Lee and Winer, 2005; Reale and Imig, 1980), which show weak tonotopy and selectivity for processing conspecific communication sounds (Norman-Haignere et al., 2015; Schneider and Woolley, 2013). Feedforward auditory information is conveyed from the MGBv to the AuC, primarily received in layer 4 (L4) but also extending to other layers (Constantinople and Bruno, 2013; Petreanu et al., 2009). Subsequently, it is projected corticofugally to downstream targets from either layer 5 (L5) or layer 6 (L6) of the AuC (Shepherd and Yamawaki, 2021), including feedback information to MGB (Happel et al., 2014; Happel et al., 2010; Homma and Bajo, 2021; Kirchgessner et al., 2020). Several studies have revealed the sophisticated inputs and the ability to perceive complex sounds of CT neurons in A1 (Clayton et al., 2021; Homma et al., 2017), suggesting the descending information flow in the core fields of the AuC possibly contributes to higher-order feedback processing of diverse auditory inputs.

It is also known that the tonotopic gradient is well preserved across all layers within the A1 (Guo et al., 2012; Montes-Lourido et al., 2021; Tischbirek et al., 2019; Winkowski and Kanold, 2013). However, all of these previous discoveries in tonotopic mapping are based on layer specificity. While the laminar structure is closely associated with functional projections in the AuC, these are not precisely identical. Neurons within the same layer can exhibit diversity in their molecular, morphological, physiological, and connectional features (Triarhou, 2021; Yarmohammadi et al., 2014), and therefore, categorizing cortical neurons based on their projection specificity can provide a deeper fundamental understanding of their functional

organization. The A1-MGB projecting neurons play an essential role in the feedforward-feedback loop of the thalamus-neocortex interplay for integrated sound information processing flow (Happel et al., 2010) and the perception of complex sounds (Clayton et al., 2021; Homma et al., 2017). However, due to technical difficulties, there has been limited understanding of the functional properties of these specific corticothalamic projecting neurons(Antunes and Malmierca, 2021; Winer et al., 2001), because they are located in deeper layers of the cortex and are more difficult to access by means of commonly-used, single-cell-resolving recording techniques such as conventional two-photon (2P) microscopy (Kobat et al., 2009; Oheim et al., 2001; Takasaki et al., 2020; Tischbirek et al., 2015).

Recent work has established a rabies-based retrograde labeling method with pathway specificity (Sun et al., 2019; Zhu et al., 2020) to circumvent the neuropil contamination problem associated with conventional 2P imaging for CT neurons. Here, using viral tracing and 2P Ca^{2+} imaging of awake head-fixed mice, we systematically revisited the functional organization in the A1, specifically targeting two types of neurons with projection specificity: TR (Zingg et al., 2017) and CT neurons (Gu et al., 2023), akin to the input and output of the AuC. The projection specificity-based approach provides detailed insight into the differences in population activity and frequency response-related topographic organization between neurons with different connectivity specificities.

Results

Pathway-specific labeling of TR and CT neurons

To label TR neurons, we used an anterograde trans-synaptic tracing strategy by injecting a Cre-recombinase-expressing AAV into the MGB, then injecting a second AAV carrying Cre-dependent GCaMP6s (AAV2/9-CaMKII-DIO-GCaMP6s) in the AuC (Figure 1A and B) (Zingg et al., 2017). Neurons labeled with AAV-GCaMP6s were observed across all layers of the AuC (Figure 1C and D). To label CT neurons, we performed retrograde tracing with a rabies virus CVS-N2c-derived vector (CVS-GCaMP6s) by injecting it into the MGB (Figure 1E). Neurons labeled with

CVS-GCaMP6s were restricted to AuC L6 (Figure 1F and G) and were then imaged by 2P Ca^{2+} imaging, in line with our recent work (Gu et al., 2023). Whole-cell patch-clamp recordings and in vivo 2P imaging showed no change in electrophysiological, morphological, or functional characteristics of CVS-labeled CT neurons (Gu et al., 2023). To locate A1, we conducted wide-field imaging in awake GCaMP6s-labeled mice, and defined that the low-frequency tone (4 kHz) elicited spatially restricted responses in the regions referred to as “low-frequency (LF) area”, and that the high-frequency tone (32 kHz) elicited responses in the regions referred to as “high-frequency (HF) area” (Figure 1H). In AAV-GCaMP6s labeled mice, we identified the locations of A1, anterior auditory field (AAF), and secondary auditory field (A2) based on the known tonotopy in mice (Figure 1H, left panel) (Issa et al., 2014; Liu et al., 2019).

It is worth noting that, in CVS-GCaMP6s-labeled (i.e., CT neurons) mice, pure tone stimulation elicited wide-field signals in only one auditory region that exhibited a tonotopic gradient (Figure 1H, right panel). To identify this region in AuC, we injected a retrograde tracing indicator cholera toxin subunit B conjugated with Alexa 555 (CTB-555) into this region, which resulted in clearly visible CTB-555-labeled cell bodies in the MGBv (Figure 1I), suggesting that CVS-GCaMP6s-labeled neurons were located in A1(Rothschild et al., 2010). When performing 2P imaging, the average power delivered to the brain was in the range of 30—120 mW, depending on the depth of imaging. To determine whether neurons labeled with the CVS retained normal response properties after deep 2P imaging—with higher laser power than that used for superficial layer imaging—we observed the broadband noise-evoked (BBN-evoked) responses of these neurons over time (days) (Figure 1— figure supplementary 1A). At 7 and 13 days after injection, we found that CVS-labeled neurons had completely normal response properties (Figure 1— figure supplementary 1B and C).

Next, we performed Ca^{2+} imaging of TR or CT neurons from A1 identified by wide-field imaging (Figure 1J). High-titer AAV1-Cre virus has been reported to anterogradely label postsynaptic neurons and also retrogradely label presynaptic

146 neurons (Zingg et al., 2017). To minimize this labeling ambiguity, we restricted the 2P
147 imaging depth of TR neurons to 200—400 μm, without imaging the neurons in L5
148 and L6, which were reciprocally connected with the MGB (Harris and Mrsic-Flogel,
149 2013). These results suggest the feasibility of our approach to label and record
150 population Ca^{2+} signals with pathway specificity at single-cell resolution in awake
151 mice.
152
153 **CT neurons exhibit no tonotopic gradient**
154 To study tonal response profiles, we delivered 330 pure tones at each focal plane (11
155 frequencies ranging from 2—40 kHz, 6 attenuation levels, 5 repetitions). We
156 determined the best frequency (BF) (Guo et al., 2012) of all tuned TR (Figure 2A) or
157 CT neurons (Figure 2B) at each 2P imaging focal plane. In total, we imaged 1041 TR
158 neurons in 5 animals. 46% were “tuned” neurons, 41% were “irregular” neurons, and
159 13% were “silent” neurons (Figure 2—figure supplementary 2A, the definitions of
160 “irregular”, “tuned”, and “silent”, see METHOD DETAILS). For CT neurons, we imaged
161 a total of 2721 neurons from 10 animals. 18% were “tuned” neurons, 57% were
162 “irregular” neurons and 25% were “silent” neurons (Figure 2—figure supplementary
163 2B).
164 Based on the BFs, we determined the median BF of all tuned neurons in each 2P
165 focal plane (e.g., Figure 2C and D) and related them to the position within the
166 wide-field imaging areas (Figure 2E and F), which were then used for computing the
167 tonotopic gradient. For TR neurons, we observed a clear tonotopic axis in the
168 organization of median BF ($R = 0.77$, $P < 0.001$; 2.13 octaves/mm; Figure 2G).
169 However, no such tonotopic gradient was observed in CT neurons ($R = 0.20$, $P = 0.21$;
170 0.21 octaves/mm; Figure 2H). Plotting the relative positions of all individual tuned TR
171 or CT neurons in each mouse revealed a significant low-to-high frequency gradient
172 from caudal to rostral for TR neurons ($R = 0.52$, $P < 0.001$; 1.76 octaves/mm; Figure 2I
173 and J), but an absence of tonotopy in CT neurons ($R = 0.079$, $P = 0.084$; 0.37
174 octaves/mm; Figure 2K and L). These results, at single-neuron resolution, confirmed
175 that the TR neuronal population does possess tonotopy, as previous reports have

shown on a coarse scale (Kalatsky et al., 2005; Wu et al., 2006).

The fraction of different BF responsive neurons among TR and CT neurons showed that both TR and CT neurons displayed no obvious pattern throughout A1 (Figure 2M). When categorized into LF or HF areas, higher proportions of TR neurons responded to low-frequency sounds in the LF areas or high-frequency sounds in the HF areas, whereas CT neurons showed no frequency preference in either area (Figure 2N and O). Note the obvious discrepancy in that the 2P imaging data here shows no tonotopic gradient of L6 CT neurons, but widefield epifluorescence imaging data shows the presence of a tonotopic gradient from the same mice (Figure 1H), which could be largely due to differences in the imaging methods and will be discussed later on.

To validate the reliability of our imaging/analysis approach, we performed control experiments that imaged the general excitatory neurons in superficial layers (Figure 2- figure supplementary 3), and the results showed a clear tonotopic gradient, which was consistent with previous findings (Bandyopadhyay et al., 2010; Romero et al., 2020; Rothschild et al., 2010; Tischbirek et al., 2019). Moreover, to definitively disentangle projection-specific properties from general layer-specific properties, we first analyzed TR neurons to see if response properties varied by depth within the superficial layers. We found no significant differences in the fraction of tuned neurons, field IQR, or BWmax between TR neurons in L2/3 versus those in L4 (Figure 2- figure supplementary 4). This suggests a degree of functional homogeneity within the thalamorecipient population across these layers. To directly test if projection identity confers distinct functional properties within the same cortical layers, we performed the crucial control of comparing TR neurons to their neighboring non-TR neurons. Our results show that TR neurons are significantly more likely to be tuned to pure tones than their neighboring non-TR excitatory neurons (Figure 2- figure supplementary 5). This finding provides direct evidence that a neuron's long-range connectivity, and not just its laminar location, is a key determinant of its response properties.

CT neurons exhibit high heterogeneity in tuning preference

Next, we performed an analysis of the BF spatial distribution within each focal plane. Examination of BF distribution among TR or CT neurons revealed that TR neurons exhibited similar frequency preference in HF or LF areas (Figure 3A), whereas CT neurons displayed high heterogeneity in their frequency preferences, regardless of LF or HF areas (Figure 3B).

To quantify the degree of BF heterogeneity, we examined BF spatial distribution at the focal plane, local, and nearest-neighboring scales. To this end, the inter-quartile range of BF (IQR_{BF}, in octaves) was calculated for all tuned neurons in each focal plane (Figure 3C and D). Quantitative analysis showed that CT neurons had higher IQR_{BF} than TR neurons across all focal planes (Figure 3C). Similarly, evaluation of LF or HF areas indicated that CT neurons had significantly higher IQR_{BF} than TR neurons in LF areas, but showed no significant difference from TR neurons in HF areas at the focal plane level (Figure 3D).

To assess tone response heterogeneity at the local scale, we then calculated IQR_{BF} for all tuned neurons within a 25 μm radius (Winkowski and Kanold, 2013; Zeng et al., 2019) around each randomly selected CT or TR neuron (Figure 3E—G). The results revealed that TR neurons also exhibited lower median IQR_{BF} than CT neurons at the local scale (Figure 3F). Consistent with the focal plane scale, CT neurons had significantly higher local IQR_{BF} than TR neurons in LF areas (Figure 3G). Unexpectedly, the local IQR_{BF} of TR neurons in HF areas was significantly higher than that of TR neurons in LF areas (Figure 3G). Further analysis across local regions revealed that the local IQR_{BF} of TR neurons followed a low-to-high gradient along the caudal-to-rostral axis ($R = 0.2655$, $P = 0.0032$; Figure 3H).

The analysis of Δfrequency (BF variability) (Bandyopadhyay et al., 2010; Zeng et al., 2019) between nearest-neighboring TR or CT neurons was consistent with results of local IQR_{BF} analysis (Figure 3I). That is, Δfrequency followed a clear gradient in the organization of TR neurons along the caudal-to-rostral axis ($R = 0.2463$, $P < 0.001$; Figure 3J). Moreover, TR neurons, but not CT neurons, displayed high IQR_{BF} in HF areas compared to LF areas (Figure 3G and I). These results suggest the relative

heterogeneity of frequency preference among CT neurons but homogeneity among TR neurons.

Receptive field properties of TR versus CT neurons

Given the above differences in the functional organization of frequency preference between TR and CT neurons, we next focused our analysis on the frequency responsive areas (FRAs) of individual neurons, as the FRAs directly reflect neuronal auditory selectivity essential for sound processing (Sadagopan and Wang, 2008). For this analysis, all tuned neurons were categorized into either a V-shaped (decreasing frequency selectivity with increasing intensity), I-shaped (narrow, level-tolerant tuning), or O-shaped (non-monotonic) FRA (Figure 4A and B). We found that a higher proportion of CT neurons was associated with V-shaped FRAs than TR neurons, whereas the proportion of CT neurons associated with I-shaped FRAs was lower than that of TR neurons (Figure 4C). By contrast, no difference was detected in the proportions of CT and TR neurons associated with O-shaped FRAs (Figure 4C).

A key feature of neuronal tuning curves is their sharpness. Common measures of sharpness in V shape are half-peak bandwidth and the "quality factor" (Q), which was obtained by dividing the BF of the neuron by a measure of tuning (Micheyl et al., 2013), the width of the tuning curve at half-peak in this study. This analysis showed that the half-peak bandwidth of CT neurons was significantly wider than that of TR neurons (Figure 4D), while the Q value of CT neurons was lower than that of TR neurons, especially in the HF areas (Figure 4E and F). Since higher Q values indicate sharper tuning of neurons, which suggests higher frequency discrimination (Micheyl et al., 2013), these results suggest that TR neurons might be responsible for finer tone discrimination.

As the bandwidth of neurons' FRA can also reflect the selectivity of overall tonal responses (Rodrigues-Dagaeff et al., 1989; Schreiner and Sutter, 1992), we examined the maximum FRA width of TR or CT neurons (Figure 4G-J). BW_{max} was defined as the maximum FRA width at any sound level. The quantitative analysis showed that the BW_{max} of TR neurons was significantly narrower than that of CT neurons, irrespective

of the FRA shape (Figure 4G). In addition, the distribution of TR neurons generally peaked at a BW_{max} of 1—2 octaves, while the distribution of CT neurons peaked at a BW_{max} of 3—4 octaves (Figure 4H). The statistical analysis showed that CT neurons had significantly higher BW_{max} than TR neurons (Figure 4I). Within LF or HF areas, TR neurons had a significantly narrower BW_{max} range than CT neurons in either area. Surprisingly, TR neurons in HF areas had a significantly lower BW_{max} than TR neurons in LF areas (Figure 4J), suggesting that the BW_{max} distribution among TR neurons might change along the caudal-to-rostral axis.

We then investigated the organization for intensity tuning, another crucial feature in auditory perception, based on the monotonicity index (MI, see Methods for details), wherein 1 indicated monotonic response increase with intensity and 0 indicated strong nonmonotonic tuning (de la Rocha et al., 2008; Sutter and Schreiner, 1995; Watkins and Barbour, 2011). The MI distribution across both TR and CT neuronal populations peaked at 1 (Figure 4K). Subsequent categorization as either monotonic or non-monotonic (using a criterion of MI = 0.5 (de la Rocha et al., 2008; Moore and Wehr, 2013), neurons with an index < 0.5 considered intensity-tuned), showed that the fraction of neurons exhibiting non-monotonic intensity response did not significantly differ between TR and CT neurons (Figure 4L). However, examination of MI values within LF or HF areas showed that a higher proportion of non-monotonic CT neurons than TR were located in LF areas, while a larger proportion of non-monotonic TR neurons were located in HF areas than in LF areas (Figure 4M). In addition, among non-monotonic neurons, TR neurons had higher MI than CT neurons, whereas monotonic TR neurons had a lower MI than monotonic CT neurons (Figure 4N). Furthermore, we note that non-monotonic CT neurons had a higher BF than monotonic CT neurons, whereas the BF was similar between monotonic and non-monotonic TR neurons (Figure 4O). Finally, BW_{max} did not significantly differ between monotonic and non-monotonic neurons in either the TR or CT populations (Figure 4P).

Discussion

A key finding in this study is that the information flow descending from A1 to the thalamus via CT neurons does not preserve tonotopy, which contrasted with the observation that the information flow ascending from the thalamus to A1 via TR neurons exhibits clear tonotopy.

Layer specific versus projection specific functional organization in A1

Previous studies have reported the existence of tonotopic gradients across all layers of A1 including L6 (Guo et al., 2012; Tischbirek et al., 2019). CT neurons labeled with CVS-GCaMP6s were restricted to A1 L6 but did not preserve tonotopy. This is because only 30 - 50% of the pyramidal cells in L6 are CT neurons (Thomson, 2010), and the neurons we image are restricted to MGB-projecting CT neurons, excluding CT neurons projecting to other downstream nuclei (Clayton et al., 2021). Using CVS-based labeling approach and 2P single-cell-resolved imaging, we successfully dissected a small fraction of CT neurons from all L6 neurons and studied the functional organization of this group of neurons.

The studies examining functional organization in AuC have mostly focused on layer specificity (Bandyopadhyay et al., 2010; Montes-Lourido et al., 2021; Rothschild et al., 2010; Tischbirek et al., 2019; Winkowski and Kanold, 2013), and these studies have provided us with a basic understanding of the tonotopy and heterogeneity of AuC. However, layer-specific representation is a relatively coarse approach. Projection specificity-based approach provides detailed insight into differences in population activity and frequency response-related topographic organization between neurons with different connectivity specificity. For example, anatomical studies of AuC in several species have identified the topographical organization of L5 corticocollicular projections (Bajo and Moore, 2005; Saldana et al., 1996; Stebbings et al., 2014). By contrast, a recent study using a pathway-specific labeling method showed that L5 corticocollicular neurons displayed a relatively weaker topological organization than the non-corticocollicular neurons in the same layer (Schmitt et al., 2023). Those studies and our data consistently support the notion that different anatomically organized projections do not necessarily transmit information with the

same topological alignment. Therefore, combining pathway-specific labeling and in vivo single-cell-resolved functional imaging could reveal unexpected fine-scale details and settle discrepancies arising from results obtained by individual methods alone.

CVS virus provides an effective means of mapping neuronal function in L6

The CVSN2c-ΔG rabies virus strain, a recently engineered self-inactivating ΔG rabies virus lacking the polymerase gene, exhibits strong neurotropism and reduced cytotoxicity (Reardon et al., 2016). Previous studies have revealed that reliable neural activity using the CVS-GCaMP6s virus can be maintained for at least 21 days, as recorded by fiber photometry (Lin et al., 2023). In acute forebrain slices, CVS-N2c-ΔG-hChR2-YFP reliably elicits action potentials in transfected cortical neurons for at least 28 days after infection (Reardon et al., 2016). Our recent studies also confirm that CVS-labeled CT neurons exhibit electrophysiological properties that are indistinguishable from those of normal neurons (Gu et al., 2023). Here, chronic 2P calcium imaging shows that CT neurons retain stable sound response properties for at least 13 days (Figure 1—figure supplementary 1). All of these studies suggest that the CVS virus-labeling method provides an effective means of mapping neuronal circuitry and manipulating neuronal activity *in vivo* in the mammalian central nervous system.

Tonotopy of CT neurons can be observed in wide-field but not 2P imaging

Our 2P imaging results are not contradictory to our wide-field epifluorescence imaging data (Figure 1), showing a tonotopy in A1 from the same mice that were later used for 2P imaging experiments. First, the source of the fluorescence signal differs between wide-field imaging and 2P imaging. Wide-field epifluorescence imaging reports all fluorescent proteins from cell bodies and neuropils across layers, whereas 2P imaging only examines fluorescent signals from the cell bodies (Scott et al., 2018). Furthermore, BF tuning from individual neurons results in a significantly closer match to wide-field mapping before removal of the neuropil contribution, thus confirming that the neuropil produces greater local homogeneity in BFs along with a

clearer global tonotopic organization (Romero et al., 2020). For L6 CT neurons, the contribution of the neuropil (dendrites) is important due to the specificity of their morphological structure: the cell bodies are located in L6, while their corresponding apical dendrites terminate in L4 (32%) or extend to L1 (68%)(Olsen et al., 2012).

Profiling of auditory features of "in-and-out" neurons in A1

At the single-neuron level, the tonotopic organization or functional distribution of adjacent neuron clusters in the AuC can be highly heterogeneous in mice (Issa et al., 2014; Tao et al., 2017; Winkowski and Kanold, 2013). Our findings in this study reveal that TR neurons exhibit more homogeneous functional and spatial distribution (Figure 3), which contrasts with some other single-cell-resolved studies in the mouse AuC (Li et al., 2017; Rothschild et al., 2010; Winkowski and Kanold, 2013). This discrepancy can also be explained by the pathway specificity, i.e., only a small fraction of neurons in the upper layers of AuC are thalamocortical recipients. It is expected that TR neurons possess high-gradient tonotopy and sharp tuning because feedforward thalamocortical projections are known to possess the same features (Guo et al., 2012; Kanold et al., 2014; Winkowski and Kanold, 2013). What is unexpected is that the same predictions based on the classical literature of functional mapping of AuC (Guo et al., 2012; Imig et al., 1977; Recanzone et al., 1999; Rothschild et al., 2010) do not apply to L6 CT neurons. This fits perfectly with a previous study, which found a transition from precise, homogenous frequency organization in L4 to coarse, diffuse organization in L2/3, suggesting that information flow exhibits diverse selectivity after cortical processing (King et al., 2018; Winkowski and Kanold, 2013).

What could be the functional meaning of this change in, or elimination of, tonotopic organization? We suggest that the descending information flow of A1-MGB projection could potentially support higher cortical functions such as higher-level feedback processing of complex (Homma et al., 2017; Malmierca et al., 2015) and behaviorally meaningful sound (Jeschke et al., 2021; Ohl et al., 2001; Wang et al., 2020; Wang et al., 2022). In addition to frequency preference, this study also

provides evidence illustrating the effects of cortical processing on response properties. For example, BW_{max}, which reflects the degree of integration of synaptic inputs from presynaptic neurons (Kratz and Manis, 2015; Li et al., 2019; Schreiner and Sutter, 1992), is 3.0 octaves in CT neurons, but only 1.3 octaves in TR neurons (Figure 4I), indicative of an increase in synaptic integration during cortical processing (Li et al., 2019).

We propose that the lack of tonotopy is an active computation, not a passive degradation. CT neurons likely pool inputs from a wide range of upstream neurons with diverse frequency preferences. This broad synaptic integration, reflected in their wider tuning bandwidth, would actively erase the fine-grained frequency map in favor of creating a different kind of representation (Brewer and Barton, 2016). This transformation away from a classic sensory map may be critical for the function of corticothalamic feedback. Instead of relaying "what" frequency was heard, the descending signal from CT neurons may convey more abstract, higher-order information, such as the behavioral relevance of a sound, predictions about upcoming sounds, or motor-related efference copy signals that are not inherently frequency-specific (Wang et al., 2020; Wang et al., 2022). The descending A1-to-MGB pathway is often considered to be modulatory, shaping thalamic responses rather than driving them directly. A modulatory signal designed to globally adjust thalamic gain or selectivity may not require, and may even be hindered by, a fine-grained topographical organization.

Conclusion

In summary, our findings fill in a knowledge gap in the auditory physiology: whereas the corticothalamic feedback projection is known to contribute to higher cognitive processing of behaviorally relevant complex sounds, the basic pure-tone map that underlies and facilitates this advanced processing remained unclear. Our results reveal that the sensory information flow descending from the A1 to the thalamus via L6 CT neurons does not arrange tonotopically. The new shift, categorizing cortical neurons based on their projection specificity, represents an advance in the

416 conceptual framework for functional organization.

417

418

419 **Figures**

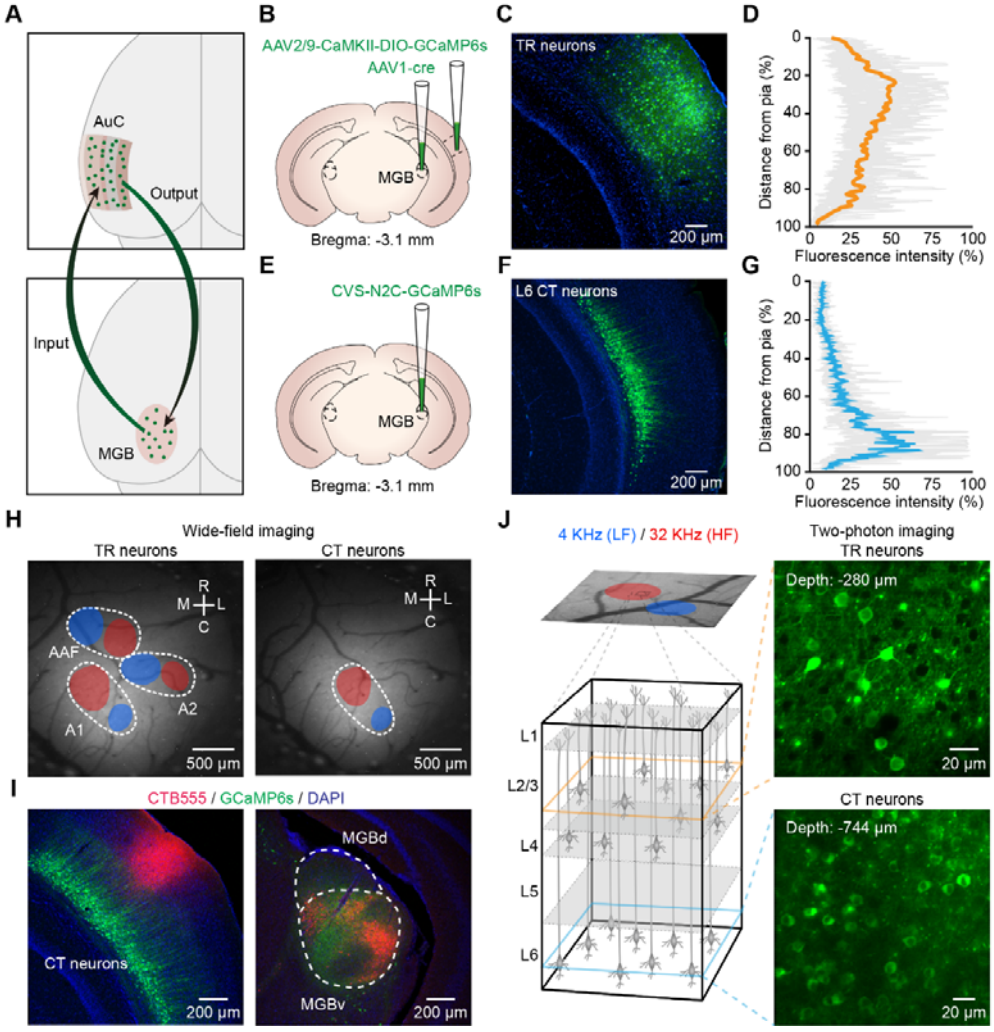

420

421 **Figure 1.** Imaging TR or CT neurons in A1 of awake mice. (**A**) Cartoon illustration of the
422 auditory thalamocortical and corticothalamic circuits. (**B**) Schematic diagram of the injection
423 site of AAV2/1-Cre in the MGB and AAV2/9-CaMKII-DIO-GCaMP6s in AuC. (**C**) Coronal slice
424 showing AAV-GCaMP6s expression in the AuC on day 21. (**D**) Fluorescence intensity of TR
425 neurons in AuC with distance from pia (0%) to the L6/WM border (100%). (**E**) Schematic
426 diagram of the injection site of CVS-GCaMP6s in the MGB. (**F**) Coronal slice showing the
427 CVS-GCaMP6s retrogradely labeled neurons in the AuC on day 7. (**G**) Fluorescence intensity
428 of CT neurons in AuC with distance from pia (0%) to the L6/WM border (100%). (**H**) Left:

429 wide-field imaging in AAV-GCaMP6s-expressing mouse (TR neurons), fluorescence response
430 to pure-tone stimulation with 4 kHz (blue area) and 32 kHz (red area). White dotted lines
431 outline the A1, A2, and AAF boundaries. Right: wide-field imaging in
432 CVS-GCaMP6s-expressing mouse (CT neurons). (**I**) Left: a fluorescent micrograph of a coronal
433 slice after CTB-555 loading guided by 2P imaging into A1 in a CVS-GCaMP6s-expressing
434 mouse. Right: micrograph of a coronal slice of the MGB from the same mouse. CTB-555
435 retrogradely labeled neurons were mainly concentrated in the MGBv. (**J**) Left: wide-field
436 imaging (in a GCaMP6s-expressing mouse) in A1, fluorescence response to pure-tone
437 stimulation with 4 kHz (low-frequency (LF) area) and 32 kHz (high-frequency (HF) area), same
438 abbreviation for all subsequent figures. Inset panels outlined by dashed boxes show the
439 magnified views of 2P imaging of TR or CT neurons. Right: examples of 2P images of TR and
440 CT neurons *in vivo*, respectively.
441

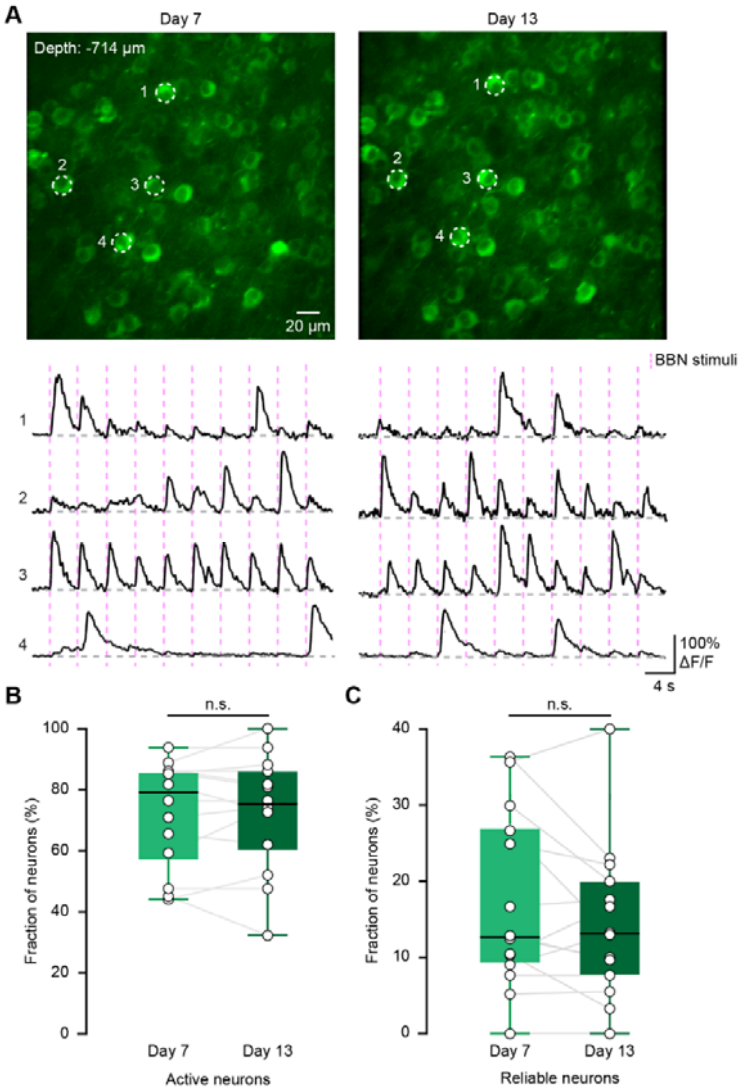

Figure 1- figure supplementary 1. Chronic *in vivo* 2P imaging of CT neurons. (**A**) Calcium imaging from L6 CT neurons in a CVS-expressing mouse, again with repeated imaging of the same focal planes on day 7 and 13 after virus injection. The dashed circle indicates the example neurons, showing fluorescence traces of neurons in the lower panel. (**B**) The comparison of the fraction of active CT neurons on day 7 and 13. *N* = 14 focal planes from 5 mice. "Day 7": 79.14\59.26–86.11%, "Day 13": 75.33\62.07–86.11%; P = 0.96, two-sided Wilcoxon signed-rank test, *P < 0.05, **P < 0.01, and ***P < 0.001, same statistics for boxplots. (**C**) The comparison of the fraction of reliable CT neurons on day 7 and 13. "Day 7": 12.70\9.09–26.67%, "Day 13": 13.19\7.69–20.00%; P = 0.53. The definitions of "active" and "reliable" neurons are provided in METHOD DETAILS.

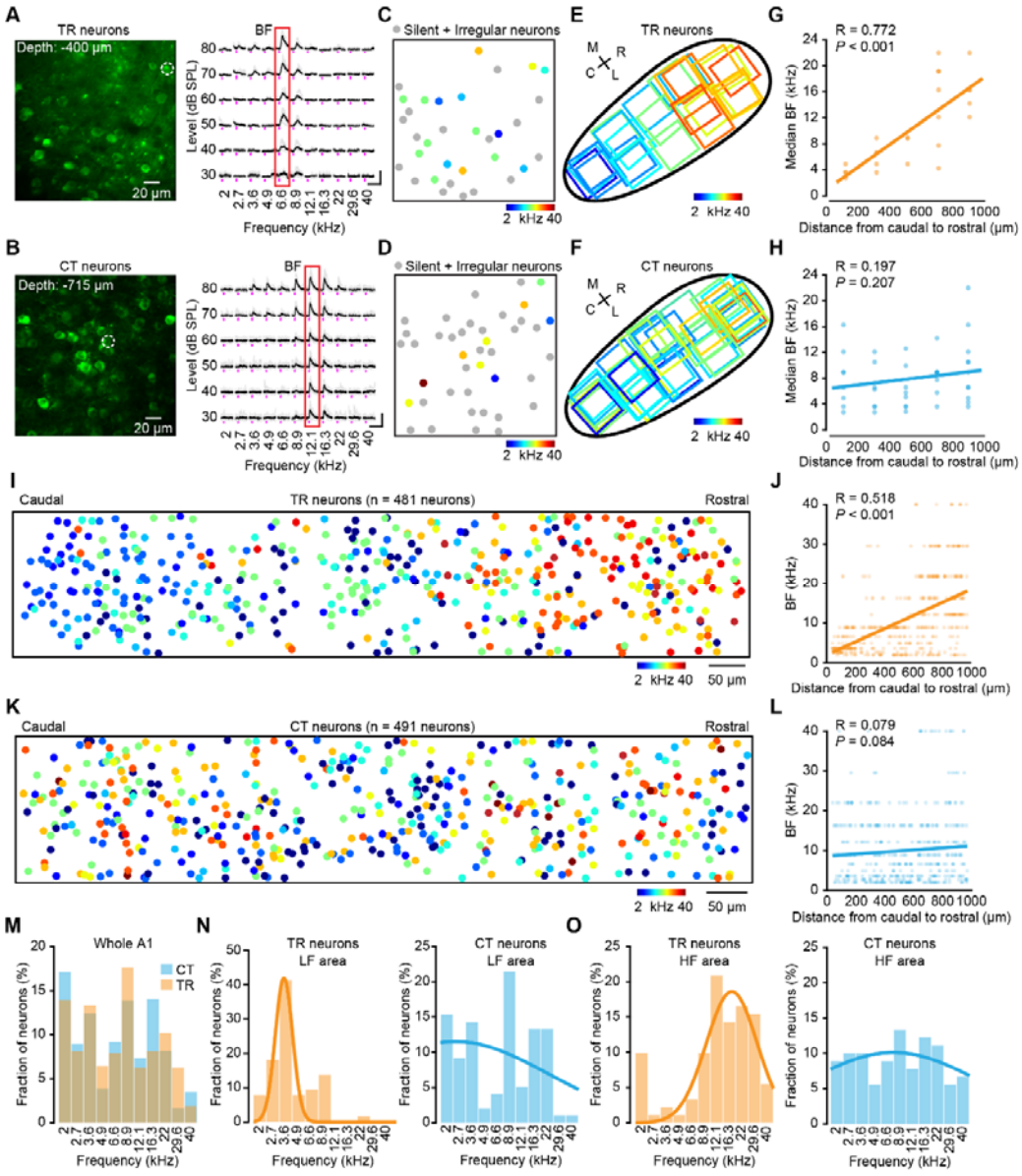

Figure 2. Tonotopic gradients of TR versus CT neurons. (**A**) Two-photon image of the focal plane used to image TR neurons in A1. The dashed circle indicates the tuned neurons. Fluorescence traces of neurons in the right panel are indicated by the dashed circle ordered according to sound frequency and level. The five traces associated with the five repeats of each stimulus are plotted in gray. The average calcium signals are plotted in black. The red outline marks the BF response of the neuron. (**B**) Same as panel (**A**) but for CT neurons in A1. (**C**) BF map of TR neurons. (**D**) BF map of CT neurons. (**E**) Schematic illustrating the recording locations of individual fields of view of TR neurons in A1. Outlines are color-coded according to the median BF response in the respective fields of view, with their BFs (kHz) color-coded

463 by the scheme below. *N* = 23 focal planes, from 5 mice. (**F**) Same as panel (**E**) but for CT
464 neurons. *N* = 40 focal planes, from 10 mice. (**G**) BF_{median} plotted against distance along the
465 tonotopic axis for TR neurons. Scatter plots showing the correlation between the cellular
466 BF_{median} values measured in the fields of view with 2P imaging and the corresponding
467 extrapolated brain surface frequencies determined by wide-field imaging of TR neurons. (**H**)
468 Same as panel (**G**) but for CT neurons. (**I**) Reconstruction of the relative spatial locations of
469 tuned TR neurons that covered the whole A1 area and color-coded according to each
470 neuron's BF. *N* = 481 neurons from 5 mice. (**J**) Plots of TR neurons' BF and their relative
471 distances along the caudal-to-rostral axis. (**K**) Same as panel **i** but for CT neurons. *N* = 491
472 neurons from 10 mice. (**L**) Same as panel (**J**) but for CT neurons. (**M**) Distribution histogram
473 of BF from all neurons in the dataset (TR: *N* = 481 neurons; CT: *N* = 491 neurons). (**N**)
474 Distribution histogram of BF neurons that were identified in the LF area by wide-field
475 imaging (TR: *N* = 116 neurons; CT: *N* = 98 neurons). (**O**) Distribution histogram of BF neurons
476 that were identified in HF area by wide-field imaging (TR: *N* = 91 neurons; CT: *N* = 90
477 neurons).
478
479

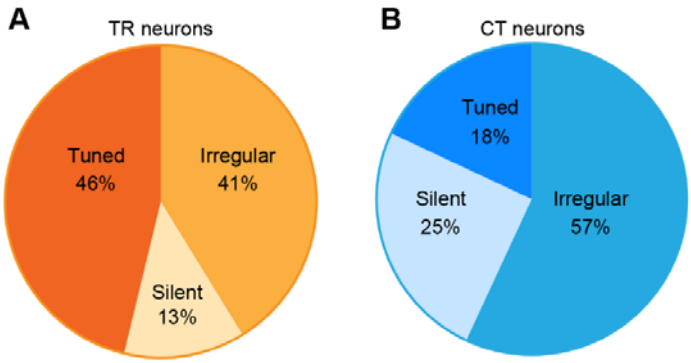

480
481 **Figure 2- figure supplementary 2.** Pie charts showing the percentage of responsive neurons
482 to pure-tone stimulation of TR and CT neurons. *N* = 5 animals for TR neurons, *N* = 10 animals
483 for CT neurons. The definitions of ''silent'' and ''irregular'' neurons are seen in METHOD
484 DETAILS.
485

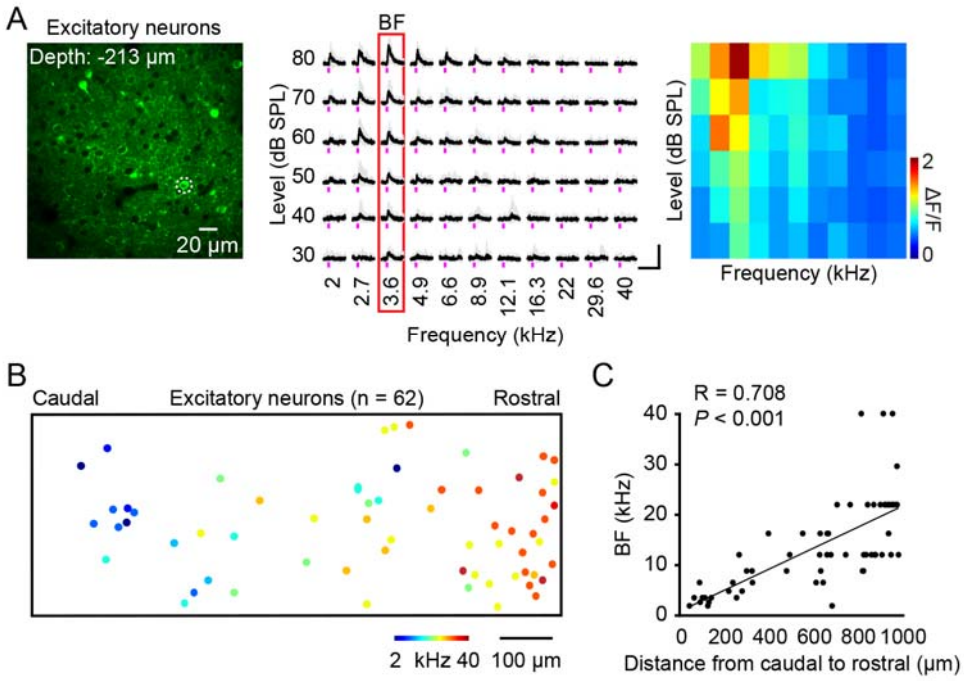

Figure 2- figure supplementary 3. Tonotopic gradients of general excitatory neurons in superficial layers. (**A**) Left panel: two-photon imaging of excitatory neurons using AAV-CaMKII-GCaMP6s labeling. The dashed circle indicates the tuned neurons. Fluorescence traces of neurons in the middle panel are indicated by the dashed circle ordered according to sound frequency and level. Middle panel: the five traces associated with the five repeats of each stimulus are plotted in gray. The average calcium signals are plotted in black. The red outline marks the BF response of the neuron. Right panel: the FRA from the tuned neurons in the left panel dashed circle. (**B**) Reconstruction of the relative spatial locations of tuned general excitatory neurons that covered the whole A1 area and are color-coded according to each neuron's BF. N = 62 neurons from one mouse. (**C**) Plots of excitatory neurons' BF and their relative distances along the caudal-to-rostral axis.

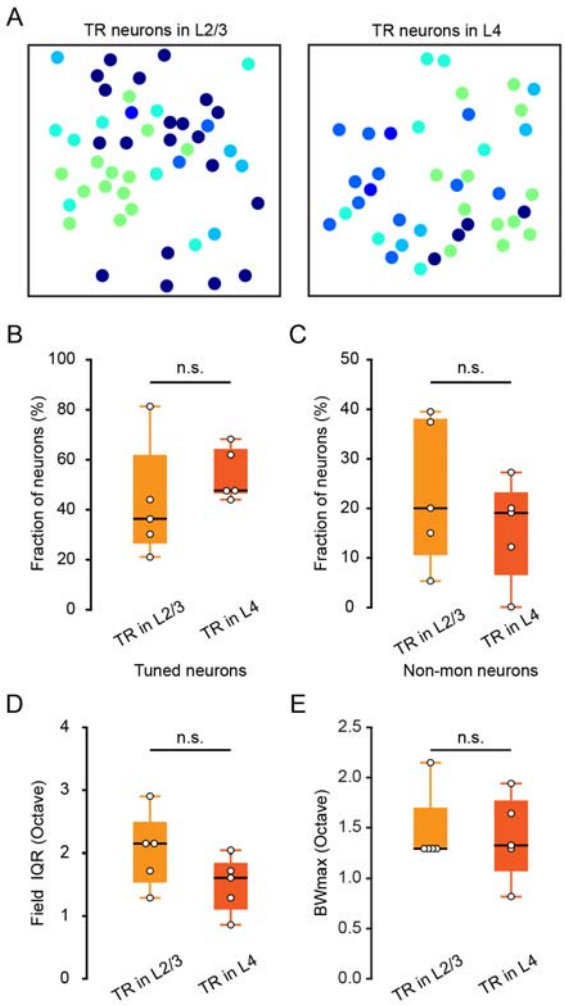

499

500 **Figure 2- figure supplementary 4.** Comparison of TR neurons across superficial layers. (**A**)
501 Spatial distribution of all tone-selective neurons in an example imaging plane of TR neurons
502 in L2/3 (left) and L4 (right) imaging area. (**B**) Comparison of the fraction of tuned TR neurons
503 in L2/3 and L4. (**C**) Comparison of the fraction of non-monotonic TR neurons in L2/3 and L4.
504 (**D**) Comparison of the field (200 µm) IQR of TR neurons in L2/3 and L4. (**E**) Comparison of
505 the BWmax of TR neurons in L2/3 and L4. N = 5 focal planes for TR neurons in L2/3, N = 5
506 focal planes for TR neurons in L4.

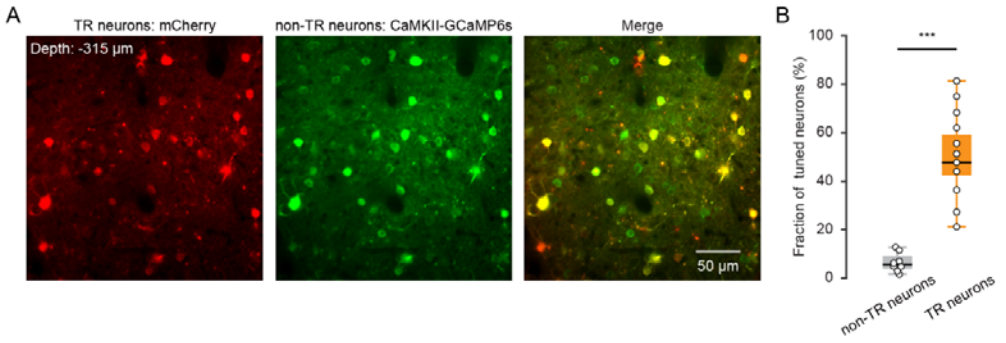

Figure 2- figure supplementary 5. Imaging pure tone responses of non-TR neurons. (**A**) Left panel: example of image with mCherry-expression in TR neurons. Injection site of AAV2/1-Cre in the MGB and AAV2/9-hSyn-DIO-mCherry in A1. Middle panel: example of image with GCaM6s-expression in general excitatory neurons. Injection site of AAV2/9-CaMKII- GCaM6s in A1. Right panel: merged image of left panel and middle panel. (**B**) Comparison of the fraction of tuned neurons among non-TR and TR neurons. non-TR neurons: N = 8 local planes from 4 mice. TR neurons: N = 11 local planes from 5 mice.

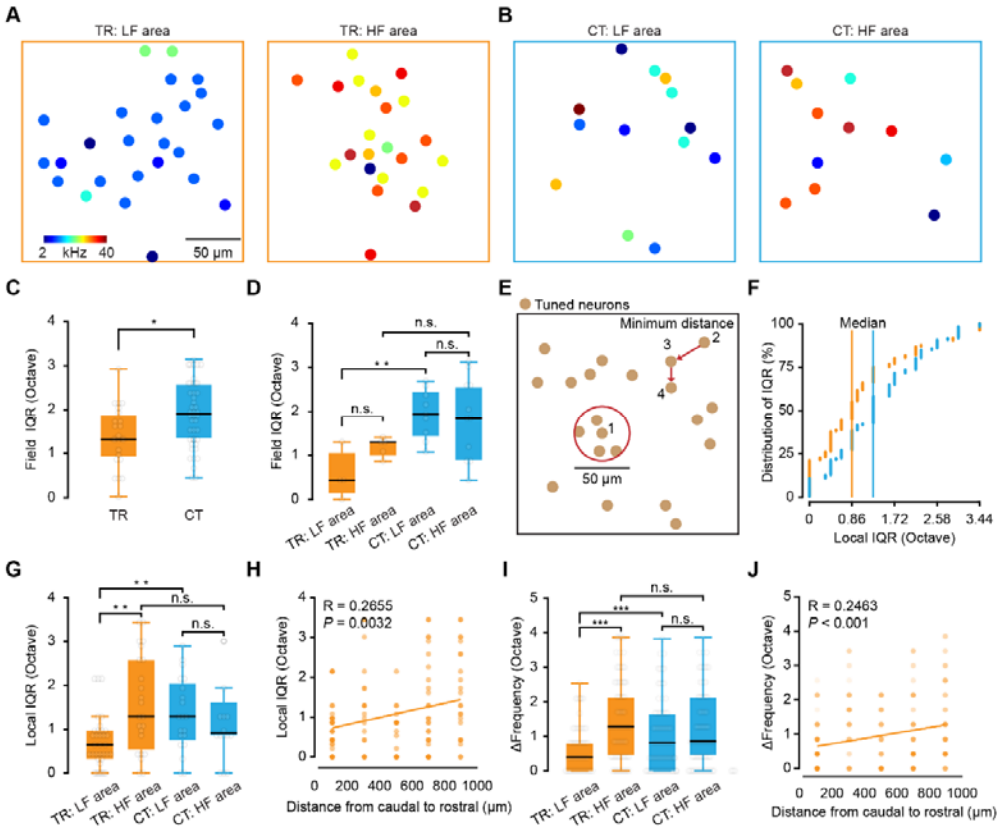

Figure 3. Heterogeneity of frequency preference in TR versus CT neurons. (**A**) Spatial distribution of all tone-selective neurons in an example imaging plane of TR neurons from LF (left) and HF (right) imaging areas. (**B**) Same as panel (**A**) but for CT neurons. BFs (kHz) color code is on panel (**A**). (**C**) Comparison of the field (200 µm) IQR of TR and CT. *N* = 23 focal planes from 5 mice for TR; *N* = 40 focal planes from 10 mice for CT. "TR": 1.29\0.91–1.88 octaves (median\25–75% percentiles, same notation for all subsequent data), "CT": 1.94\1.29–2.58 octaves. *P* = 0.016, two-sided Wilcoxon rank-sum test, **P* < 0.05, ***P* < 0.01, and ****P* < 0.001, same statistics for boxplots. (**D**) Comparison of the field IQR of TR and CT neurons in LF and HF areas. LF area: *N* = 4 focal planes from 3 mice for TR; *N* = 9 focal planes from 5 mice for CT. HF area: *N* = 5 focal planes from 5 mice for TR; *N* = 11 focal planes from 10 mice for CT. "TR: LF area": 0.43\0.22–0.86 octaves, "TR: HF area": 1.29\1.02–1.32 octaves, "CT: LF area": 1.94\1.45–2.42 octaves, "CT: HF area": 1.83\0.94–2.58 octaves. *P* (TR: LF area, HF area) = 0.11, *P* (CT: LF area, HF area) = 0.82, *P* (LF area: TR, CT) = 0.0084, *P* (HF area: TR, CT) = 0.25. (**E**) Cartoon showing how the local and minimum percentages were computed. (**F**) Cumulative percentage plot displaying local (25 µm radius) IQR around each neuron of TR

and CT. Median local IQR_{BF} of TR neurons = 0.86 octaves, *N* = 120 local planes from 5 mice; median local IQR_{BF} of CT neurons = 1.29 octaves, *N* = 105 local planes from 10 mice. (**G**) Comparison of the local (25 µm radius) IQR of TR and CT neurons in LF and HF areas. LF area: *N* = 34 local planes for TR; *N* = 20 local planes for CT. HF area: *N* = 23 local planes for TR; *N* = 16 local planes for CT. "TR: LF area": 0.65\0.32–0.97 octaves, "TR: HF area": 1.29\0.54–2.58 octaves, "CT: LF area": 1.29\0.75–2.04 octaves, "CT: HF area": 0.91\0.86–1.61 octaves. *P* (TR: LF area, HF area) = 0.0021, *P* (CT: LF area, HF area) = 0.69, *P* (LF area: TR, CT) = 0.0057, *P* (HF area: TR, CT) = 0.34. (**H**) Local IQR_{BF} plotted against distance along the tonotopic axis for TR neurons. (**I**) Comparison of the minimum distance Δ Frequency of TR and CT neurons in LF and HF area. LF area: *N* = 116 paired neurons for TR; *N* = 87 paired neurons for CT. HF area: *N* = 91 paired neurons for TR; *N* = 78 paired neurons for CT. "TR: LF area": 0.43\0.00–0.86 octaves, "TR: HF area": 0.86\0.00–1.72 octaves, "CT: LF area": 0.43\0.00–1.29 octaves, "CT: HF area": 0.43 \0.00–1.29 octaves. *P* (TR: LF area, HF area) = 4.25e-04, *P* (CT: LF area, HF area) = 0.79, *P* (LF area: TR, CT) = 0.18, *P* (HF area: TR, CT) = 0.025. (**J**) Δ Frequency plotted against distance along the tonotopic axis for TR neurons.

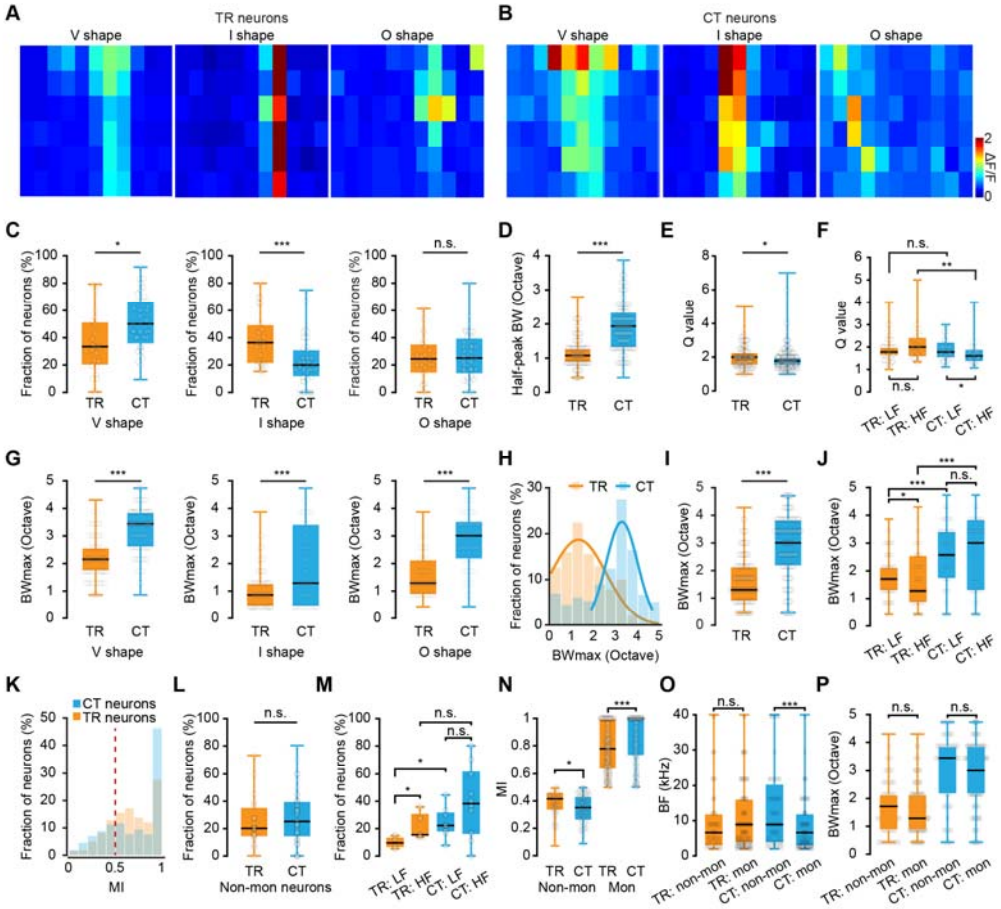

Figure 4. Receptive field properties of TR versus CT neurons. (**A**) One representative FRA from a specific type of TR neuron. Types are V shape, I shape, and O shape. See text for further details. The X-axis represents 11 pure tone frequencies, and the Y-axis represents 6 sound intensities. (**B**) One representative FRA from a specific type of CT neuron. (**C**) Comparison of fraction of neurons from V, I, and O shaped neurons in TR and CT. (**D**) Comparison of half-peak bandwidth of V-shaped TR and CT neurons. *N* = 190 neurons from 5 mice for TR; *N* = 249 neurons from 10 mice for CT. "TR": 1.08\0.86–1.29 octaves, "CT": 1.94\1.29–2.37 octaves. *P* = 4.86e-29. (**E**) Comparison of Q value (bandwidth of BF/half bandwidth) of V-shaped TR and CT neurons. *N* = 190 neurons from 5 mice for TR; *N* = 249 neurons from 10 mice for CT. "TR": 2.00\1.50–2.29, "CT": 1.78\1.50–2.00. *P* = 0.035. (**F**) Comparison of the Q value of V-shaped TR and CT neurons in LF and HF areas. LF area: *N* = 56 neurons for TR; *N* = 49 neurons for CT. HF area: *N* = 37 neurons for TR; *N* = 41 neurons for CT. "TR: LF area": 1.78\1.60–2.00, "TR: HF area": 2.00\1.58–2.43, "CT: LF area": 1.78\1.50–2.22, "CT: HF area": 1.60\1.33–1.88. *P* (TR: LF area, HF area) = 0.20, *P* (CT: LF area,

HF area) = 0.032, *P* (LF area: TR, CT) = 0.88, *P* (HF area: TR, CT) = 0.0032. (**G**) Comparison of maximum bandwidth (BW_{max}) from V, I, and O shaped neurons in TR and CT. V shape: *N* = 190 neurons for TR, *N* = 249 neurons for CT; "TR": 2.15\1.72–2.58 octaves, "CT": 3.44\2.58–3.87 octaves; *P* = 4.18e-29. I shape: *N* = 174 neurons for TR, *N* = 112 neurons for CT; "TR": 0.86\0.43–1.29 octaves, "CT": 1.29\0.43–3.44 octaves; *P* = 4.66e-05. O shape: *N* = 117 neurons for TR, *N* = 130 neurons for CT; "TR": 1.29\0.86–2.15 octaves, "CT": 3.01\2.15–3.44 octaves; *P* = 4.30e-19. (**H**) Distribution histogram of BW_{max} from all neurons in the dataset. (**I**) Comparison of the BW_{max} of TR and CT neurons. *N* = 481 neurons from 5 mice for TR, *N* = 491 neurons from 10 mice for CT; "TR": 1.29\0.86–2.15 octaves, "CT": 3.01\2.15–3.87 octaves; *P* = 1.89e-51. (**J**) Comparison of the BW_{max} of TR and CT neurons in LF and HF areas. LF area: *N* = 116 neurons for TR; *N* = 98 neurons for CT. HF area: *N* = 91 neurons for TR; *N* = 90 neurons for CT. "TR: LF area": 1.72\1.29–2.15, "TR: HF area": 1.29\0.86–2.47, "CT: LF area": 2.58\1.72–3.44, "CT: HF area": 3.01\1.29–3.87. *P* (TR: LF area, HF area) = 0.034, *P* (CT: LF area, HF area) = 0.92, *P* (LF area: TR, CT) = 2.44e-08, *P* (HF area: TR, CT) = 2.28e-06. (**K**) Distribution of the monotonicity index (MI) of TR and CT neurons. (**L**) Comparison of the fraction of non-monotonic neurons of TR and CT. *N* = 23 focal planes from 5 mice for TR, *N* = 40 focal planes from 10 mice for CT; "TR": 20.00%\12.92–31.49%, "CT": 25.00%\14.58–40.00%; *P* = 0.33. (**M**) Comparison of the fraction of non-monotonic neurons of TR and CT in LF and HF areas. LF area: *N* = 4 focal planes from 3 mice for TR; *N* = 9 focal planes from 5 mice for CT. HF area: *N* = 5 focal planes from 5 mice for TR; *N* = 11 focal planes from 10 mice for CT. "TR: LF area": 9.55%\6.08–13.50%, "TR: HF area": 15.38%\14.66–29.38%; "CT: LF area": 22.22%\17.59–31.67%, "CT: HF area": 38.18%\16.67–60.00%; *P* (TR: LF area, HF area) = 0.032, *P* (CT: LF area, HF area) = 0.19, *P* (LF area: TR, CT) = 0.016, *P* (HF area: TR, CT) = 0.17. (**N**) Comparison of the MI of non-monotonic and monotonic neurons in TR and CT. Non-mon: *N* = 107 neurons for TR, *N* = 128 neurons for CT; "TR": 0.42\0.33–0.47, "CT": 0.35\0.26–0.44; *P* = 7.03e-04. Mon: *N* = 374 neurons for TR, *N* = 363 neurons for CT; "TR": 0.78\0.63–1.00, "CT": 1.00\0.73–1.00; *P* = 6.19e-11. (**O**) Comparison of the BF between monotonic and non-monotonic neurons in TR and CT. TR: *N* = 107 neurons for non-mon, *N* = 374 neurons for mon; "non-mon": 6.60\2.93–12.10 kHz, "mon": 8.90\3.60–16.30 kHz; *P* = 0.69. CT: *N* = 128 neurons for non-mon, *N* = 363 neurons for mon; "non-mon": 8.90\3.60–19.15 kHz, "mon":

6.60\2.70–12.10 kHz; *P* = 1.64e-04. (**P**) Comparison of the BW_{max} between monotonic and non-monotonic neurons in TR and CT. TR: *N* = 107 neurons for non-mon, *N* = 374 neurons for mon; “non-mon”: 1.72\0.86–2.15 octaves, “mon”: 1.29\0.86–2.15 octaves; *P* = 0.92. CT: *N* = 128 neurons for non-mon, *N* = 363 neurons for mon; “non-mon”: 3.44\2.15–3.87 octaves, “mon”: 3.01\2.15–3.87 octaves; *P* = 0.052.

Materials and methods

Key resources table

Reagent type (species) or resource	Designation	Source or reference	Identifiers	Additional information
Genetic reagent (Mus musculus)	Mouse: C57BL/6J	Beijing HFK	RRID:IMSR_JAX:000664	https://www.jax.org/
Recombinant DNA reagent	AAV2/1-hSyn-Cre-WPRE-hGH polyA	BrainVTA	PT-0136	
Recombinant DNA reagent	AAV2/9-CaMKII-DIO-GCaMP6s-WPRE-hGHpA	BrainVTA	PT-0071	
Recombinant RNA reagent	CVS-N2c-ΔG-GCaM6s	BrainCase Co., Ltd.	BC-RV-CVS715	
Peptide, recombinant protein	Alexa Fluor 555-conjugated Cholera Toxin Subunit B	Invitrogen	C34776	
Chemical compound	DAPI	Sigma-Aldrich	Cat# D9542	
Software, algorithm	Matlab	Mathworks	N/A	https://www.mathworks.com/
Software, algorithm	LabVIEW	National Instruments	N/A	https://www.ni.com/zh-cn.html
Software, algorithm	Igor Pro	Wavemetrics	N/A	https://www.wavemetr

				ics.com/
Software, algorithm	Prism	GraphPad	N/A	https://www.graphpad.com/
Other	UHU Super Glue	DETAI	N/A	
Other	Sun Medical Super Bond C & B Kit Bonding Kit	Super-Bond	N/A	

Animals

C57BL/6J male mice (2–3 months old) were provided by the Laboratory Animal Center at the Third Military Medical University. The mice were housed in a temperature- and humidity-controlled room on a cycle of 12-h light/dark (lights off at 19:00) with free access to food and water. All animal procedures were approved by the Animal Care Committee of the Third Military Medical University and were performed in accordance with the principles outlined in the National Institutes of Health Guide for the Care and Use of Laboratory Animals.

Virus injections and confocal imaging

Mice were anesthetized with 1% to 2% isoflurane in pure oxygen and placed in a stereotactic frame (Beijing Zhongshi Dichuang Technology Development Co., Ltd.). A warm heating pad was used to keep the animals at a proper body temperature (36.5°C to 37.5°C). To achieve TR neurons labeling, a Cre-expressing AAV (AAV2/1-hSyn-Cre-WPRE-hGH polyA, titer ≥ 1E+13vg/ml, PT-0136, BrainVTA) was injected into the MGB (AP -3.1 mm, ML 2.0 mm, DV -2.8 mm from dura) and DIO-expressing AAV (AAV2/9-CaMKII-DIO-GCaMp6s-WPRE-hGH pA, PT-0071, BrainVTA) was injected into the AuC (AP -3.1 mm, ML 3.8 mm, DV -1.4 mm from dura with manipulator tilted 25° from the z-axis). For CT neuron labeling, the CVS virus (CVS-N2c-ΔG-GCaM6s), packaged by BrainCase Co., Ltd., Shenzhen, China, was

injected into the MGB. In all the injections, approximately 100 nL of virus was performed. After injection, the pipette was held in place for 10 min before retraction. Tissue glue (3M Animal Care Products, Vetbond) was used for bonding the scalp incision.

Mice were killed for histology 4 weeks after AAV injection or 7 days after CVS injection. For slice preparation, mice were perfused transcardially with 4% paraformaldehyde in phosphate-buffered saline. Brains were postfixed in 4% paraformaldehyde overnight at 4 °C and cut into 50 µm sections on a cryostat microtome (Thermo Fisher, NX50, Waltham, MA). Mounted sections were imaged on a scanning confocal microscope (TCS SP5, Leica).

Auditory stimulation

Sound stimuli were delivered by an ED1 electrostatic speaker driver and a free-field ES1 speaker (both from Tucker Davis Technologies). During experiments, the speaker was put at a distance of ~6 cm to the left ear of the animal. The sound stimulus was produced by a custom-written, LabVIEW-based program (LabVIEW 2012, National Instruments) and transformed to analogue voltage through a PCI6731 card (National Instruments). All the data were obtained at 1 MHz via a data acquisition device (USB-6361, National Instruments) and examined by our custom-made LabVIEW program. For BBN (BBN, bandwidth 0–50 kHz), the sound level was ~65 dB sound pressure level (SPL). We generated a waveform segment of BBN and used the same waveform segment for all experiments involving BBN.

For functional mapping of TR and CT neurons, sequences of randomly ordered pure tones with 11 frequencies (2–40 kHz) at 6 attenuation levels (30–80 dB SPL) were used. Each frequency-attenuation combination was presented 5–8 times. Background noise generated by the recording hardware, especially the resonance scanner of the 2P microscope, was measured to be below < 30 dB SPL for the relevant frequency range. The use of a specialized sound-proof enclosure with wedge-shaped acoustic foam was implemented to significantly reduce external noise interference. These strategies ensured that auditory stimuli were delivered under

653 highly controlled, low-noise conditions, thereby enhancing the reliability and
654 accuracy of the neural response measurements obtained throughout the study. As
655 described in our previous reports, low frequencies (<1 kHz) were major components
656 of background noise. With a spectral density of ~33 dB/sqrt (Hz), the peak of
657 background noise was below 1 kHz. Neither visible light nor other sensory stimuli
658 were present. The duration of a sound stimulus (tone or BBN) was 100 ms.
659
660 ***In vivo* wide-field epifluorescence imaging**
661 A homemade binocular microscope (BM01, SIBET, CAS) with a 4X, 0.2 NA objective
662 (Olympus) was used to record wide-field fluorescence images in the mouse cortex for
663 establishing the reference cortical map of A1. A light-emitting diode (470 nm,
664 M470L4, Thorlabs) was used for blue illumination. Green fluorescence passed
665 through a filter cube was measured at 10 Hz with a sCMOS camera (Zyla 4.2, Andor
666 Technology). Mice injected with AAV-GCaM6s or CVS-GCaM6s were used to
667 functionally identify the region of A1. The mouse was anesthetized by isoflurane and
668 kept on a warm plate (37.5°C). A piece of bone (~5 mm × 5 mm) was removed and
669 replaced by a coverslip (3 mm in diameter). To localize A1, two pure tones (4 and 32
670 kHz) were repeatedly presented 20 times at an interval of 6 s.
671 We observed that pure tone stimulation evoked wide-field signals in only one
672 auditory region in CVS-GCaM6s mice. To confirm the region, we used the criterion
673 that the ventral part of the medial geniculate body (MGBv) is connecting with A1.
674 Injections were performed under visual guidance using 2P excitation. In the
675 experiment, we inserted the electrode into the cortical region at a depth of ~500 µm
676 below the surface. We used Alexa Fluor 555-conjugated cholera toxin subunit B (CTB)
677 as the neural tracer and injected the fluorescent CTB solution with 0.5% in phosphate
678 buffer by pressure (700 mbar) for 15min. Seven days after the fluorescent CTB
679 injection, the mice were anesthetized with pentobarbital (1.0 g/kg ip). The brain was
680 first dissected out and then it was immersed with 4% paraformaldehyde overnight.
681 To visualize fluorescent tracers, a consecutive series of coronal or horizontal sections
682 (50 µm thick) were prepared using a sliding cryotome, and then all sections were

683 mounted onto glass slides and imaged with a stereoscope (Olympus).

684

685 **Two-photon Ca^{2+} imaging in A1**

686 For 2P imaging in head-fixed awake mice, we removed the skin and muscles over the
687 right A1 after local lidocaine injection under isoflurane anesthesia (1–2%). A
688 custom-made plastic chamber (head post) designed for head-fixed mouse
689 experiments was then glued to the skull with cyanoacrylic glue (UHU). After recovery
690 from surgery for 3 days, the mouse underwent head-fixation training for 3–5 days
691 (from 1 to 4 h per day). After head-fixation training, mice gradually adapted to this
692 posture and were able to sit comfortably for 4 h. On the recording day, a small
693 craniotomy was performed under local anesthesia. Then the field of interest was
694 determined by comparing the wide-field map with the blood vessel patterns to
695 ensure A1 was imaged.

696 Two-photon imaging was performed with a custom-built 2P microscope system
697 based on a 12.0 kHz resonant scanner (model "LotosScan 1.0", Suzhou Institute of
698 Biomedical Engineering and Technology). Two-photon excitation light was delivered
699 by a mode-locked Ti: Sa laser (model "Mai-Tai DeepSee", Spectra Physics), and a
700 40×/0.8 numerical aperture (NA) water immersion objective (Nikon) was used for
701 imaging. For Ca^{2+} imaging experiments, the excitation wavelength was set to 920 nm.
702 The typical size of the field of view (FOV) was ~200 µm × 200 µm. The average power
703 delivered to the brain was in the range of 30–120 mW, depending on the depth of
704 imaging.

705

706 **Chronic 2P Ca^{2+} imaging in L6**

707 For chronic 2P imaging, A circular cranial window (2.5 mm diameter coverslip) was
708 implanted over the right AuC after head-post implantation. To this end, the muscle
709 and skull fascia above the temporal skull were removed after local lidocaine (2%)
710 injection. Afterward, a custom-made plastic chamber was fixed to the skull with
711 dental cement (Superbond, Sun Medical Co., Ltd.) and a small craniotomy (~2.7 mm
712 in diameter, the center point: AP: -3.0 mm, ML: -4.5 mm) was performed. The dura

was removed, and the craniotomy was polished to match the size of the coverslip. A coverslip was carefully placed on top of the cortex with mild compression by tweezers. The coverslip was sealed with UV-curing dental cement (Tetric N-flow, Ivoclar Co., Ltd.). Antibiotics (Cefazolin, 500 mg/kg, North China Pharmaceutical Group Corporation) were administered before surgery, as well as until 3 days after surgery. 3 days of post-surgery recovery were needed before head-fixation training.

Continuous 2P Ca^{2+} imaging was performed on day 7 and 13. To minimize the bleaching of cells, we used low laser illumination in the deep imaging, based on high-quality imaging of CT neurons with CVS labeling strategy. The repeated imaging FOVs were identified on consecutive days based on superficial blood vessels and nearby blood vessels, then further refined by visually matching reference images acquired from precedent days.

QUANTIFICATION AND STATISTICAL ANALYSIS

Data were analyzed using custom-written software in LabVIEW 2012 (National Instruments), Igor Pro 5.0 (Wavemetrics), Image 1.51 (NIH), Prism 8.4 (GraphPad) and MATLAB 2014a (MathWorks).

Wide-field imaging data analysis

In each mouse, the recorded cortical images were first down sampled from the original 750 × 1200 pixels to 75 × 120 pixels. After that, the frames recorded with sound stimuli were averaged across 20 trials. To enhance the signal-to-noise ratio, spatial averaging was conducted over 5 × 5 pixels by a matrix filter, and temporal averaging was conducted with three consecutive images. The pre-processed images were then temporally normalized to obtain the relative changes in fluorescence (f) pixel-by-pixel. With the baseline fluorescence (f0) obtained by averaging the images of 800 ms before sound stimulation, the relative fluorescence changes of each pixel were calculated as $\Delta f/f = (f - f0)/f0$. The normalized images are shown on a color-coded scale to visualize the relative fluorescence changes ($\Delta f/f$) in the cortex.

743 **Two-photon imaging data analysis**

744 To correct motion-related artifacts in imaging data, a frame-by-frame alignment
745 algorithm was used to minimize the sum of squared intensity differences between
746 each frame image and a template, which was the average of the selected image
747 frames. To extract fluorescence signals, neurons were visually identified, and drawing
748 regions of interest (ROIs) based on fluorescence intensity was performed.
749 Fluorescence changes (f) were calculated by averaging the corresponding pixel values
750 for each ROI. Relative fluorescence changes $\Delta f/f = (f-f0)/f0$ were calculated as Ca^{2+}
751 signals, where the baseline fluorescence f0 was estimated as the 25th percentile of
752 the entire fluorescence recording. To calculate the amplitude of sound-evoked Ca^{2+}
753 transients, we performed automatic Ca^{2+} transient detection based on threshold
754 criteria regarding peak amplitude and rising rate. The noise level was set to be 3
755 times the standard deviation of the baseline (window length: 1 s). The peak
756 amplitude and the rate of rising of the Ca^{2+} signals were calculated to determine
757 whether it was a true transient. The trace of the detected Ca^{2+} transient was first
758 extracted by exponential infinite impulse response (IIR) filtering (window length: 200
759 ms) and then subtracted from the original signal. The residual fluorescence trace was
760 used as the baseline for the next transient detection, similar to previously published
761 peeling approaches.

762

763 **Sound-evoked Ca^{2+} responsiveness**

764 **BBN-evoked Ca^{2+} responsiveness**

765 For data from chronic Ca^{2+} imaging, we tracked the same FOV based on the last
766 training day. We removed the outer ~10% of the image from each ROI to account for
767 edge effects or imaging deviation. The success rate was defined as the fraction of
768 sound-evoked responses during 10 consecutive BBN stimuli. Note that "Active"
769 neurons showed clear Ca^{2+} transients during the entire recording duration, including
770 spontaneous and BBN-evoked responses. The neurons with a success rate ≥ 50%
771 were defined as "Reliable" neurons among active neurons.

772

Pure tone-evoked Ca^{2+} responsiveness

The frequency response area (FRA) of each ROI was constructed from the 55 average responses to all of the unique frequency-attenuation combinations. The frequency tuning curves were constructed by plotting the average values (and the s.e.m.) of the calcium signal amplitudes from single trials for each frequency tested. If more than one area of contiguous frequency-level combinations remained, the largest one was defined as the FRA. The amplitude of a Ca^{2+} signal was determined as the average value for a period of 200 ms around the peak of the calcium transient. The baseline value was calculated for a period of 100 ms before the onset of the auditory stimulus. Pure tone frequencies that induced response amplitudes higher than half of the maximal response were defined as effective frequencies.

"Irregular" neurons were characterized by exhibiting spontaneous activity patterns that were highly variable and inconsistent in their responses to sound stimulation. These neurons showed no clear or predictable firing pattern. "Tuned" neurons represented a subset of responsive neurons that demonstrated significant and consistent selectivity for specific auditory stimuli. These neurons exhibited well-defined frequency tuning or preference, responding robustly to certain sound features while showing diminished activity to others. "Silent" neurons were operationally defined as those that remained completely inactive throughout the entire recording period, which extended beyond 30 minutes. These neurons showed no detectable spontaneous firing or evoked responses during the experiments. For tuned neurons, the best frequency (BF) was defined as the sound frequency associated with the highest response averaged across all sound levels.

FRAs that exhibited a pattern of decreasing frequency selectivity as sound intensity increased were categorized as V-shaped, reflecting a broadening of the receptive field at higher stimulus levels. This shape indicates that the neuron responds to a wider range of frequencies when the stimulus becomes more intense, suggesting a loss of tuning precision at higher intensities. In contrast, FRAs that maintained consistent frequency selectivity across increasing sound intensities were classified as I-shaped, signifying a stable tuning profile regardless of stimulus

amplitude. This pattern implies that the neuron's frequency preference remains sharply defined and resistant to intensity-dependent modulation. Additionally, FRAs that demonstrated responsiveness confined to a narrow range of both sound frequencies and intensities were designated as O-shaped, provided that their peak neural response did not occur at the maximum intensity tested. This classification suggests a limited dynamic range and a preference for intermediate stimulus conditions. Maximum bandwidth (BW_{max}) was defined as the maximum FRA width at any level.

To compare the BF heterogeneity, we analyzed the BF distribution in fixed-size analysis windows. The BF heterogeneity was quantified by the interquartile range (IQR) of the distribution. For filed IQR, if less than 5 neurons were within a 100 μm radius (including the center neuron), no IQR was calculated(Schmitt et al., 2023). For Large-scale analysis, imaging regions in separate mice were aligned with each other according to the caudal-to-rostral gradient that was identifiable in the wide-field images.

The monotonicity index (MI) characterizes the strength of a neuron's intensity tuning. We defined MI as the neuron's response at maximum intensity (80 dB) divided by its maximum response (Moore and Wehr, 2013; Sutter and Schreiner, 1995). An MI of 1 indicates no intensity tuning; an MI near zero indicates very strong intensity tuning.

Statistics

To compare data between groups, we used the nonparametric Wilcoxon rank sum test (unpaired), and Wilcoxon signed-rank test (paired) to determine statistical significance ($P < 0.05$) between them. In the text, summarized data are presented as the median\25th–75th percentiles. In the figures, the data presented in the box-and-whisker plot indicate the median (center line), 25th and 75th percentiles (Q1 and Q3), i.e., IQR (box), Q1-1.5 × IQR and Q3 + 1.5 × IQR (whiskers), and all other data with error bars are presented as the mean ± s.e.m.

Acknowledgments

The authors would like to thank Jia Lou for the cartoon art and figure layout. This work was supported by grants from the National Key R&D Program of China (2021YFA0805000), the National Natural Science Foundation of China (32300937, T2241002, 31925018, 32127801), the Jiangsu Provincial Big Science Facility Initiative (BM2022010), and Guangxi Science and Technology Base & Talents Fund (GUIKE AD22035948). X.C. is a member of the CAS Center for Excellence in Brain Science and Intelligence Technology.

Additional information

Funding

Funder	Grant reference number	Author
National Key R&D Program of China	2021YFA0805000	Xiaowei Chen
National Natural Science Foundation of China	32300937	Jianxiong Zhang
National Natural Science Foundation of China	T2241002	Jianxiong Zhang
National Natural Science Foundation of China	31925018	Xiaowei Chen
National Natural Science Foundation of China	32127801	Xiaowei Chen
Jiangsu Provincial Big Science Facility Initiative	BM2022010	Hongbo Jia
Guangxi Science and Technology Base & Talents Fund	GUIKE AD22035948	Xiaowei Chen

Author contributions

X.C. and H.J. conceived the project. X.C., JX.Z. and Y.Z. designed the experiments. M.G. performed the experiments with the help of R.L., K.L., X.W. and JH.Z.; X.C., H.J., Y.Z., S.L., JX.Z., and M.G. devised the data analysis methods; M.G., S.L., Yun.Z., X.L., C.Z. and JX.Z. performed the data analysis; JX.Z., H.J., Y.Z. and X.C. inspected the data and

evaluated the findings; M.G., JX.Z., Y.Z., F.O., X.C. and H.J. wrote the manuscript with the help from all authors.

Author ORCIDs

Xiaowei Chen: https://orcid.org/0000-0003-0906-6666
Jianxiong Zhang: https://orcid.org/0000-0003-2245-8752
Yi Zhou: https://orcid.org/0000-0002-2623-8960

Ethics

All experiments were approved by the Animal Care Committee of the Third Military Medical University (Approval number: AMUWEC20230061).

Additional files

Data availability

Wide-field imaging and two-photon imaging are available upon request from the corresponding author. Source data underlying Figs. 2–4 is available as a Source data file. No datasets that require mandatory deposition into a public database were generated during the current study. Source data are provided in this paper.

Code availability

The codes supporting the current study have not been deposited in a public repository, but are available from the corresponding author upon request.

References

Andersen RA, Knight PL, Merzenich MM. 1980. The thalamocortical and corticothalamic connections of AI, AII, and the anterior auditory field (AAF) in the cat: evidence for two largely segregated systems of connections. *Journal of Comparative Neurology* 194: 663-701. DIO: https://doi.org/10.1002/cne.901940312, PMID: 7451688

878 Antunes FM, Malmierca MS. 2021. Corticothalamic Pathways in Auditory Processing:
879 Recent Advances and Insights From Other Sensory Systems. *Front Neural Circuits* 15:
880 721186. DIO: https://doi.org/10.3389/fncir.2021.721186, PMID: 34489648

881 Bajo VM, Moore DR. 2005. Descending projections from the auditory cortex to the inferior
882 colliculus in the gerbil, Meriones unguiculatus. *Journal of Comparative Neurology* 486: 101-16.
883 DIO: https://doi.org/10.1002/cne.20542, PMID: 15844210

884 Bandyopadhyay S, Shamma SA, Kanold PO. 2010. Dichotomy of functional organization
885 in the mouse auditory cortex. *Nat Neurosci* 13: 361-8. DIO: https://doi.org/10.1038/nn.2490,
886 PMID: 20118924

887 Bizley JK, Nodal FR, Nelken I, King AJ. 2005. Functional organization of ferret auditory
888 cortex. *Cerebral Cortex* 15: 1637-53. DIO: https://doi.org/10.1093/cercor/bhi042, PMID:
889 15703254

890 Brewer AA, Barton B. 2016. Maps of the Auditory Cortex. *Annual Review of Neuroscience*
891 39: 385-407. DIO: https://doi.org/10.1146/annurev-neuro-070815-014045, PMID: 27145914

892 Budinger E, Heil P, Scheich H. 2000. Functional organization of auditory cortex in the
893 Mongolian gerbil (Meriones unguiculatus). IV. Connections with anatomically characterized
894 subcortical structures. *European Journal of Neuroscience* 12: 2452-74. DIO:
895 https://doi.org/10.1046/j.1460-9568.2000.00143.x, PMID: 10947822

896 Clayton KK, Williamson RS, Hancock KE, Tasaka GI, Mizrahi A, Hackett TA, Polley DB.
897 2021. Auditory Corticothalamic Neurons Are Recruited by Motor Preparatory Inputs. *Current*
898 *Biology* 31: 310-321 e5. DIO: https://doi.org/10.1016/j.cub.2020.10.027, PMID: 33157020

899 Clopton BM, Winfield JA, Flammino FJ. 1974. Tonotopic organization: review and

900 analysis. *Brain Research* 76: 1-20. DIO: https://doi.org/10.1016/0006-8993(74)90509-5, PMID:
901 4367399

902 Constantinople CM, Bruno RM. 2013. Deep cortical layers are activated directly by
903 thalamus. *Science* 340: 1591-4. DIO: https://doi.org/10.1126/science.1236425, PMID:
904 23812718

905 de la Rocha J, Marchetti C, Schiff M, Reyes AD. 2008. Linking the response properties of
906 cells in auditory cortex with network architecture: cotuning versus lateral inhibition. *Journal of*
907 *Neuroscience* 28: 9151-63. DIO: https://doi.org/10.1523/JNEUROSCI.1789-08.2008, PMID:
908 18784296

909 Gu M, Li X, Liang S, Zhu J, Sun P, He Y, Yu H, Li R, Zhou Z, Lyu J, Li SC, Budinger E,
910 Zhou Y, Jia H, Zhang J, Chen X. 2023. Rabies virus-based labeling of layer 6 corticothalamic
911 neurons for two-photon imaging in vivo. *iScience* 26: 106625. DIO:
912 https://doi.org/10.1016/j.isci.2023.106625, PMID: 37250327

913 Guo W, Chambers AR, Darrow KN, Hancock KE, Shinn-Cunningham BG, Polley DB.
914 2012. Robustness of cortical topography across fields, laminae, anesthetic states, and
915 neurophysiological signal types. *Journal of Neuroscience* 32: 9159-72. DIO:
916 https://doi.org/10.1523/JNEUROSCI.0065-12.2012, PMID: 22764225

917 Hackett TA, Stepniewska I, Kaas JH. 1998. Subdivisions of auditory cortex and ipsilateral
918 cortical connections of the parabelt auditory cortex in macaque monkeys. *Journal of*
919 *Comparative Neurology* 394: 475-95. DIO:
920 https://doi.org/10.1002/(sici)1096-9861(19980518)394:4<475::aid-cne6>3.0.co;2-z, PMID:
921 9590556

Happel MF, Deliano M, Handschuh J, Ohl FW. 2014. Dopamine-modulated recurrent corticoefferent feedback in primary sensory cortex promotes detection of behaviorally relevant stimuli. *Journal of Neuroscience* 34: 1234-47. DIO: https://doi.org/10.1523/JNEUROSCI.1990-13.2014, PMID: 24453315

Happel MF, Jeschke M, Ohl FW. 2010. Spectral integration in primary auditory cortex attributable to temporally precise convergence of thalamocortical and intracortical input. *Journal of Neuroscience* 30: 11114-27. DIO: https://doi.org/10.1523/JNEUROSCI.0689-10.2010, PMID: 20720119

Harris KD, Mrsic-Flogel TD. 2013. Cortical connectivity and sensory coding. *Nature* 503: 51-8. DIO: https://doi.org/10.1038/nature12654, PMID: 24201278

Homma NY, Bajo VM. 2021. Lemniscal Corticothalamic Feedback in Auditory Scene Analysis. *Frontiers in Neuroscience* 15: 723893. DIO: https://doi.org/10.3389/fnins.2021.723893, PMID: 34489635

Homma NY, Happel MFK, Nodal FR, Ohl FW, King AJ, Bajo VM. 2017. A Role for Auditory Corticothalamic Feedback in the Perception of Complex Sounds. *Journal of Neuroscience* 37: 6149-6161. DIO: https://doi.org/10.1523/JNEUROSCI.0397-17.2017, PMID: 28559384

Humphries C, Liebenthal E, Binder JR. 2010. Tonotopic organization of human auditory cortex. *Neuroimage* 50: 1202-11. DIO: https://doi.org/10.1016/j.neuroimage.2010.01.046, PMID: 20096790

Imig TJ, Ruggero MA, Kitzes LM, Javel E, Brugge JF. 1977. Organization of auditory cortex in the owl monkey (Aotus trivirgatus). *Journal of Comparative Neurology* 171: 111-28.

944 DIO: https://doi.org/10.1002/cne.901710108, PMID: 401509

945 Issa JB, Haeffele BD, Agarwal A, Bergles DE, Young ED, Yue DT. 2014. Multiscale
946 optical Ca2+ imaging of tonal organization in mouse auditory cortex. *Neuron* 83: 944-59. DIO:
947 https://doi.org/10.1016/j.neuron.2014.07.009, PMID: 25088366

948 Jasmin K, Lima CF, Scott SK. 2019. Understanding rostral-caudal auditory cortex
949 contributions to auditory perception. *Nature Reviews Neuroscience* 20: 425-434. DIO:
950 https://doi.org/10.1038/s41583-019-0160-2, PMID: 30918365

951 Jeschke M, Ohl FW, Wang X. 2021. Effects of Cortical Cooling on Sound Processing in
952 Auditory Cortex and Thalamus of Awake Marmosets. *Front Neural Circuits* 15: 786740. DIO:
953 https://doi.org/10.3389/fncir.2021.786740, PMID: 35069125

954 Jones EG. 2001. The thalamic matrix and thalamocortical synchrony. *Trends in*
955 *Neurosciences* 24: 595-601. DIO: https://doi.org/10.1016/s0166-2236(00)01922-6, PMID:
956 11576674

957 Kajikawa Y, de La Mothe L, Blumell S, Hackett TA. 2005. A comparison of neuron
958 response properties in areas A1 and CM of the marmoset monkey auditory cortex: tones and
959 broadband noise. *Journal of Neurophysiology* 93: 22-34. DIO:
960 https://doi.org/10.1152/jn.00248.2004, PMID: 15342713

961 Kalatsky VA, Polley DB, Merzenich MM, Schreiner CE, Stryker MP. 2005. Fine functional
962 organization of auditory cortex revealed by Fourier optical imaging. *Proceedings of the*
963 *National Academy of Sciences of the United States of America* 102: 13325-30. DIO:
964 https://doi.org/10.1073/pnas.0505592102, PMID: 16141342

965 Kanold PO, Nelken I, Polley DB. 2014. Local versus global scales of organization in

966 auditory cortex. *Trends in Neurosciences* 37: 502-10. DIO:
967 https://doi.org/10.1016/j.tins.2014.06.003, PMID: 25002236

968 King AJ, Teki S, Willmore BDB. 2018. Recent advances in understanding the auditory
969 cortex. *F1000Res* 7 DIO: https://doi.org/10.12688/f1000research.15580.1, PMID: 30345008

970 Kirchgessner MA, Franklin AD, Callaway EM. 2020. Context-dependent and dynamic
971 functional influence of corticothalamic pathways to first- and higher-order visual thalamus.
972 *Proceedings of the National Academy of Sciences of the United States of America* 117:
973 13066-13077. DIO: https://doi.org/10.1073/pnas.2002080117, PMID: 32461374

974 Kobat D, Durst ME, Nishimura N, Wong AW, Schaffer CB, Xu C. 2009. Deep tissue
975 multiphoton microscopy using longer wavelength excitation. *Optics Express* 17: 13354-13364.
976 DIO: https://doi.org/10.1364/Oe.17.013354, PMID: WOS:000268843700009

977 Kratz MB, Manis PB. 2015. Spatial organization of excitatory synaptic inputs to layer 4
978 neurons in mouse primary auditory cortex. *Front Neural Circuits* 9: 17. DIO:
979 https://doi.org/10.3389/fncir.2015.00017, PMID: 25972787

980 Lee CC. 2013. Thalamic and cortical pathways supporting auditory processing. *Brain and*
981 *Language* 126: 22-8. DIO: https://doi.org/10.1016/j.bandl.2012.05.004, PMID: 22728130

982 Lee CC, Schreiner CE, Imaizumi K, Winer JA. 2004. Tonotopic and heterotopic projection
983 systems in physiologically defined auditory cortex. *Neuroscience* 128: 871-87. DIO:
984 https://doi.org/10.1016/j.neuroscience.2004.06.062, PMID: 15464293

985 Lee CC, Winer JA. 2005. Principles governing auditory cortex connections. *Cerebral*
986 *Cortex* 15: 1804-14. DIO: https://doi.org/10.1093/cercor/bhi057, PMID: 15800026

987 Li H, Liang F, Zhong W, Yan L, Mesik L, Xiao Z, Tao HW, Zhang LI. 2019. Synaptic

Mechanisms for Bandwidth Tuning in Awake Mouse Primary Auditory Cortex. *Cerebral Cortex* 29: 2998-3009. DIO: https://doi.org/10.1093/cercor/bhy165, PMID: 30010857

Li J, Zhang J, Wang M, Pan J, Chen X, Liao X. 2017. Functional imaging of neuronal activity of auditory cortex by using Cal-520 in anesthetized and awake mice. *Biomed Opt Express* 8: 2599-2610. DIO: https://doi.org/10.1364/boe.8.002599, PMID: 28663893

Lin KZ, Li L, Ma WY, Yang X, Han ZP, Luo NS, Wang J, Xu FQ. 2023. A rabies virus-based toolkit for efficient retrograde labeling and monosynaptic tracing. *Neural Regen Res* 18: 1827-1833. DIO: https://doi.org/10.4103/1673-5374.358618, PMID: 36751812

Liu J, Whiteway MR, Sheikhattar A, Butts DA, Babadi B, Kanold PO. 2019. Parallel Processing of Sound Dynamics across Mouse Auditory Cortex via Spatially Patterned Thalamic Inputs and Distinct Areal Intracortical Circuits. *Cell Rep* 27: 872-885 e7. DIO: https://doi.org/10.1016/j.celrep.2019.03.069, PMID: 30995483

Malmierca MS, Anderson LA, Antunes FM. 2015. The cortical modulation of stimulus-specific adaptation in the auditory midbrain and thalamus: a potential neuronal correlate for predictive coding. *Front Syst Neurosci* 9: 19. DIO: https://doi.org/10.3389/fnsys.2015.00019, PMID: 25805974

Merzenich MM, Brugge JF. 1973. Representation of the cochlear partition of the superior temporal plane of the macaque monkey. *Brain Research* 50: 275-96. DIO: https://doi.org/10.1016/0006-8993(73)90731-2, PMID: 4196192

Merzenich MM, Kaas JH, Roth GL. 1976. Auditory cortex in the grey squirrel: tonotopic organization and architectonic fields. *Journal of Comparative Neurology* 166: 387-401. DIO: https://doi.org/10.1002/cne.901660402, PMID: 1270613

Micheyl C, Schrater PR, Oxenham AJ. 2013. Auditory frequency and intensity discrimination explained using a cortical population rate code. *PLoS Computational Biology* 9: e1003336. DIO: https://doi.org/10.1371/journal.pcbi.1003336, PMID: 24244142

Montes-Lourido P, Kar M, David SV, Sadagopan S. 2021. Neuronal selectivity to complex vocalization features emerges in the superficial layers of primary auditory cortex. *PLoS Biology* 19: e3001299. DIO: https://doi.org/10.1371/journal.pbio.3001299, PMID: 34133413

Moore AK, Wehr M. 2013. Parvalbumin-expressing inhibitory interneurons in auditory cortex are well-tuned for frequency. *Journal of Neuroscience* 33: 13713-23. DIO: https://doi.org/10.1523/JNEUROSCI.0663-13.2013, PMID: 23966693

Morel A, Garraghty PE, Kaas JH. 1993. Tonotopic organization, architectonic fields, and connections of auditory cortex in macaque monkeys. *Journal of Comparative Neurology* 335: 437-59. DIO: https://doi.org/10.1002/cne.903350312, PMID: 7693772

Nelken I, Bizley JK, Nodal FR, Ahmed B, Schnupp JW, King AJ. 2004. Large-scale organization of ferret auditory cortex revealed using continuous acquisition of intrinsic optical signals. *Journal of Neurophysiology* 92: 2574-88. DIO: https://doi.org/10.1152/jn.00276.2004, PMID: 15152018

Norman-Haignere S, Kanwisher NG, McDermott JH. 2015. Distinct Cortical Pathways for Music and Speech Revealed by Hypothesis-Free Voxel Decomposition. *Neuron* 88: 1281-1296. DIO: https://doi.org/10.1016/j.neuron.2015.11.035, PMID: 26687225

Oheim M, Beaurepaire E, Chaigneau E, Mertz J, Charpak S. 2001. Two-photon microscopy in brain tissue: parameters influencing the imaging depth. *Journal of Neuroscience Methods* 111: 29-37. DIO: https://doi.org/10.1016/s0165-0270(01)00438-1, PMID: 11574117

Ohga S, Tsukano H, Horie M, Terashima H, Nishio N, Kubota Y, Takahashi K, Hishida R, Takebayashi H, Shibuki K. 2017. DIO: https://doi.org/10.1101/226100,

Ohl FW, Scheich H, Freeman WJ. 2000. Topographic analysis of epidural pure-tone-evoked potentials in gerbil auditory cortex. *Journal of Neurophysiology* 83: 3123-32. DIO: https://doi.org/10.1152/jn.2000.83.5.3123, PMID: 10805706

Ohl FW, Scheich H, Freeman WJ. 2001. Change in pattern of ongoing cortical activity with auditory category learning. *Nature* 412: 733-6. DIO: https://doi.org/10.1038/35089076, PMID: 11507640

Olsen SR, Bortone DS, Adesnik H, Scanziani M. 2012. Gain control by layer six in cortical circuits of vision. *Nature* 483: 47-52. DIO: https://doi.org/10.1038/nature10835, PMID: 22367547

Pardi MB, Vogenstahl J, Dalmay T, Spano T, Pu DL, Naumann LB, Kretschmer F, Sprekeler H, Letzkus JJ. 2020. A thalamocortical top-down circuit for associative memory. *Science* 370: 844-848. DIO: https://doi.org/10.1126/science.abc2399, PMID: 33184213

Petreanu L, Mao T, Sternson SM, Svoboda K. 2009. The subcellular organization of neocortical excitatory connections. *Nature* 457: 1142-5. DIO: https://doi.org/10.1038/nature07709, PMID: 19151697

Polley DB, Read HL, Storace DA, Merzenich MM. 2007. Multiparametric auditory receptive field organization across five cortical fields in the albino rat. *Journal of Neurophysiology* 97: 3621-38. DIO: https://doi.org/10.1152/jn.01298.2006, PMID: 17376842

Reale RA, Imig TJ. 1980. Tonotopic organization in auditory cortex of the cat. *Journal of Comparative Neurology* 192: 265-91. DIO: https://doi.org/10.1002/cne.901920207, PMID:

7400399

Reardon TR, Murray AJ, Turi GF, Wirblich C, Croce KR, Schnell MJ, Jessell TM, Losonczy A. 2016. Rabies Virus CVS-N2c(DeltaG) Strain Enhances Retrograde Synaptic Transfer and Neuronal Viability. *Neuron* 89: 711-24. DIO: https://doi.org/10.1016/j.neuron.2016.01.004, PMID: 26804990

Recanzone GH, Schreiner CE, Sutter ML, Beitel RE, Merzenich MM. 1999. Functional organization of spectral receptive fields in the primary auditory cortex of the owl monkey. *Journal of Comparative Neurology* 415: 460-81. DIO: https://doi.org/10.1002/(sici)1096-9861(19991227)415:4<460::aid-cne4>3.0.co;2-f, PMID: 10570456

Rodrigues-Dagaeff C, Simm G, De Ribaupierre Y, Villa A, De Ribaupierre F, Rouiller EM. 1989. Functional organization of the ventral division of the medial geniculate body of the cat: evidence for a rostro-caudal gradient of response properties and cortical projections. *Hearing Research* 39: 103-25. DIO: https://doi.org/10.1016/0378-5955(89)90085-3, PMID: 2737959

Romero S, Hight AE, Clayton KK, Resnik J, Williamson RS, Hancock KE, Polley DB. 2020. Cellular and Widefield Imaging of Sound Frequency Organization in Primary and Higher Order Fields of the Mouse Auditory Cortex. *Cerebral Cortex* 30: 1603-1622. DIO: https://doi.org/10.1093/cercor/bhz190, PMID: 31667491

Rothschild G, Nelken I, Mizrahi A. 2010. Functional organization and population dynamics in the mouse primary auditory cortex. *Nat Neurosci* 13: 353-60. DIO: https://doi.org/10.1038/nn.2484, PMID: 20118927

Sadagopan S, Wang X. 2008. Level invariant representation of sounds by populations of

1076 neurons in primary auditory cortex. *Journal of Neuroscience* 28: 3415-26. DIO:
1077 https://doi.org/10.1523/JNEUROSCI.2743-07.2008, PMID: 18367608

1078 Saldana E, Feliciano M, Mugnaini E. 1996. Distribution of descending projections from
1079 primary auditory neocortex to inferior colliculus mimics the topography of intracollicular
1080 projections. *Journal of Comparative Neurology* 371: 15-40. DIO:
1081 https://doi.org/10.1002/(SICI)1096-9861(19960715)371:1<15::AID-CNE2>3.0.CO;2-O, PMID:
1082 8835717

1083 Schmitt TTX, Andrea KMA, Wadle SL, Hirtz JJ. 2023. Distinct topographic organization
1084 and network activity patterns of corticocollicular neurons within layer 5 auditory cortex. *Front*
1085 *Neural Circuits* 17: 1210057. DIO: https://doi.org/10.3389/fncir.2023.1210057, PMID:
1086 37521334

1087 Schneider DM, Woolley SM. 2013. Sparse and background-invariant coding of
1088 vocalizations in auditory scenes. *Neuron* 79: 141-52. DIO:
1089 https://doi.org/10.1016/j.neuron.2013.04.038, PMID: 23849201

1090 Schreiner CE, Sutter ML. 1992. Topography of excitatory bandwidth in cat primary
1091 auditory cortex: single-neuron versus multiple-neuron recordings. *Journal of Neurophysiology*
1092 68: 1487-502. DIO: https://doi.org/10.1152/jn.1992.68.5.1487, PMID: 1479426

1093 Scott BB, Thiberge SY, Guo C, Tervo DGR, Brody CD, Karpova AY, Tank DW. 2018.
1094 Imaging Cortical Dynamics in GCaMP Transgenic Rats with a Head-Mounted Widefield
1095 Macroscope. *Neuron* 100: 1045-1058 e5. DIO: https://doi.org/10.1016/j.neuron.2018.09.050,
1096 PMID: 30482694

1097 Shepherd GMG, Yamawaki N. 2021. Untangling the cortico-thalamo-cortical loop: cellular

1098 pieces of a knotty circuit puzzle. *Nature Reviews Neuroscience* 22: 389-406. DIO:
1099 https://doi.org/10.1038/s41583-021-00459-3, PMID: 33958775

1100 Simon E, Perrot X, Mertens P. 2009. [Functional anatomy of the cochlear nerve and the
1101 central auditory system]. *Neuro-Chirurgie* 55: 120-6. DIO:
1102 https://doi.org/10.1016/j.neuchi.2009.01.017, PMID: 19304300

1103 Smith KR, Wever EG. 1949. The problem of stimulation deafness; the functional and
1104 histological effects of a high-frequency stimulus. *Journal of Experimental Psychology* 39:
1105 238-41. DIO: https://doi.org/10.1037/h0061044, PMID: 18125722

1106 Stebbings KA, Lesicko AM, Llano DA. 2014. The auditory corticocollicular system:
1107 molecular and circuit-level considerations. *Hearing Research* 314: 51-9. DIO:
1108 https://doi.org/10.1016/j.heares.2014.05.004, PMID: 24911237

1109 Stiebler I, Neulist R, Fichtel I, Ehret G. 1997. The auditory cortex of the house mouse:
1110 left-right differences, tonotopic organization and quantitative analysis of frequency
1111 representation. *J Comp Physiol A* 181: 559-71. DIO: https://doi.org/10.1007/s003590050140,
1112 PMID: 9449817

1113 Sun L, Tang Y, Yan K, Yu J, Zou Y, Xu W, Xiao K, Zhang Z, Li W, Wu B, Hu Z, Chen K, Fu
1114 ZF, Dai J, Cao G. 2019. Differences in neurotropism and neurotoxicity among retrograde viral
1115 tracers. *Molecular Neurodegeneration* 14: 8. DIO: https://doi.org/10.1186/s13024-019-0308-6,
1116 PMID: 30736827

1117 Sutter ML, Schreiner CE. 1995. Topography of intensity tuning in cat primary auditory
1118 cortex: single-neuron versus multiple-neuron recordings. *Journal of Neurophysiology* 73:
1119 190-204. DIO: https://doi.org/10.1152/jn.1995.73.1.190, PMID: 7714564

Takasaki K, Abbasi-Asl R, Waters J. 2020. Superficial Bound of the Depth Limit of Two-Photon Imaging in Mouse Brain. *eNeuro* 7 DIO: https://doi.org/10.1523/ENEURO.0255-19.2019, PMID: 31907211

Tani T, Abe H, Hayami T, Banno T, Miyakawa N, Kitamura N, Mashiko H, Ichinohe N, Suzuki W. 2018. Sound Frequency Representation in the Auditory Cortex of the Common Marmoset Visualized Using Optical Intrinsic Signal Imaging. *eNeuro* 5 DIO: https://doi.org/10.1523/ENEURO.0078-18.2018, PMID: 29736410

Tao C, Zhang G, Zhou C, Wang L, Yan S, Tao HW, Zhang LI, Zhou Y, Xiong Y. 2017. Diversity in Excitation-Inhibition Mismatch Underlies Local Functional Heterogeneity in the Rat Auditory Cortex. *Cell Rep* 19: 521-531. DIO: https://doi.org/10.1016/j.celrep.2017.03.061, PMID: 28423316

Thomas H, Tillein J, Heil P, Scheich H. 1993. Functional organization of auditory cortex in the mongolian gerbil (Meriones unguiculatus). I. Electrophysiological mapping of frequency representation and distinction of fields. *European Journal of Neuroscience* 5: 882-97. DIO: https://doi.org/10.1111/j.1460-9568.1993.tb00940.x, PMID: 8281300

Thomson AM. 2010. Neocortical layer 6, a review. *Front Neuroanat* 4: 13. DIO: https://doi.org/10.3389/fnana.2010.00013, PMID: 20556241

Tischbirek C, Birkner A, Jia H, Sakmann B, Konnerth A. 2015. Deep two-photon brain imaging with a red-shifted fluorometric Ca2+ indicator. *Proceedings of the National Academy of Sciences of the United States of America* 112: 11377-82. DIO: https://doi.org/10.1073/pnas.1514209112, PMID: 26305966

Tischbirek CH, Noda T, Tohmi M, Birkner A, Nelken I, Konnerth A. 2019. In Vivo

1142 Functional Mapping of a Cortical Column at Single-Neuron Resolution. *Cell Rep* 27:
1143 1319-1326 e5. DIO: https://doi.org/10.1016/j.celrep.2019.04.007, PMID: 31042460

1144 Triarhou LC. 2021. Pre-Brodmann pioneers of cortical cytoarchitectonics I: Theodor
1145 Meynert, Vladimir Betz and William Bevan-Lewis. *Brain Structure and Function* 226: 49-67.
1146 DIO: https://doi.org/10.1007/s00429-020-02168-6, PMID: 33165657

1147 Wang M, Liao X, Li R, Liang S, Ding R, Li J, Zhang J, He W, Liu K, Pan J, Zhao Z, Li T,
1148 Zhang K, Li X, Lyu J, Zhou Z, Varga Z, Mi Y, Zhou Y, Yan J, Zeng S, Liu JK, Konnerth A,
1149 Nelken I, Jia H, Chen X. 2020. Single-neuron representation of learned complex sounds in the
1150 auditory cortex. *Nature Communications* 11: 4361. DIO:
1151 https://doi.org/10.1038/s41467-020-18142-z, PMID: 32868773

1152 Wang M, Liu K, Pan J, Li J, Sun P, Zhang Y, Li L, Guo W, Xin Q, Zhao Z, Liu Y, Zhou Z,
1153 Lyu J, Zheng T, Han Y, Zhang C, Liao X, Zeng S, Jia H, Chen X. 2022. Brain-wide projection
1154 reconstruction of single functionally defined neurons. *Nature Communications* 13: 1531. DIO:
1155 https://doi.org/10.1038/s41467-022-29229-0, PMID: 35318336

1156 Watkins PV, Barbour DL. 2011. Rate-level responses in awake marmoset auditory cortex.
1157 *Hearing Research* 275: 30-42. DIO: https://doi.org/10.1016/j.heares.2010.11.011, PMID:
1158 21145961

1159 Winer JA, Diehl JJ, Larue DT. 2001. Projections of auditory cortex to the medial
1160 geniculate body of the cat. *Journal of Comparative Neurology* 430: 27-55. DIO, PMID:
1161 11135244

1162 Winer JA, Miller LM, Lee CC, Schreiner CE. 2005. Auditory thalamocortical transformation:
1163 structure and function. *Trends in Neurosciences* 28: 255-63. DIO:

https://doi.org/10.1016/j.tins.2005.03.009, PMID: 15866200

Winkowski DE, Kanold PO. 2013. Laminar transformation of frequency organization in auditory cortex. *J Neurosci* 33: 1498-508. DIO: https://doi.org/10.1523/jneurosci.3101-12.2013, PMID: 23345224

Wu GK, Li P, Tao HW, Zhang LI. 2006. Nonmonotonic synaptic excitation and imbalanced inhibition underlying cortical intensity tuning. *Neuron* 52: 705-15. DIO: https://doi.org/10.1016/j.neuron.2006.10.009, PMID: 17114053

Yarmohammadi H, Mahmoudi Nezhad GS, Dalfardi B, Ghanizadeh A. 2014. Theodor Meynert (1833-1892). *Journal of Neurology* 261: 1647-8. DIO: https://doi.org/10.1007/s00415-013-7077-x, PMID: 23963472

Zeng HH, Huang JF, Chen M, Wen YQ, Shen ZM, Poo MM. 2019. Local homogeneity of tonotopic organization in the primary auditory cortex of marmosets. *Proceedings of the National Academy of Sciences of the United States of America* 116: 3239-3244. DIO: https://doi.org/10.1073/pnas.1816653116, PMID: 30718428

Zhu X, Lin K, Liu Q, Yue X, Mi H, Huang X, He X, Wu R, Zheng D, Wei D, Jia L, Wang W, Manyande A, Wang J, Zhang Z, Xu F. 2020. Rabies Virus Pseudotyped with CVS-N2C Glycoprotein as a Powerful Tool for Retrograde Neuronal Network Tracing. *Neurosci Bull* 36: 202-216. DIO: https://doi.org/10.1007/s12264-019-00423-3, PMID: 31444652

Zingg B, Chou XL, Zhang ZG, Mesik L, Liang F, Tao HW, Zhang LI. 2017. AAV-Mediated Anterograde Transsynaptic Tagging: Mapping Corticocollicular Input-Defined Neural Pathways for Defense Behaviors. *Neuron* 93: 33-47. DIO: https://doi.org/10.1016/j.neuron.2016.11.045, PMID: 27989459

1186